Quantitative gas property measurements by filtered Rayleigh scattering: A review

Cody R Ground[1], Robin L Hunt[1], Gregory J Hunt[2]

[1] Hypersonic Airbreathing Propulsion Branch, NASA Langley Research Center, 12 Langley Blvd. Hampton, VA 23681, United States of America

[2] William & Mary, PO Box 8763 Williamsburg, VA 23187 United States of America

E-mail: cody.r.ground@nasa.gov

March 2023

Abstract.

Filtered Rayleigh scattering (FRS) is a laser-based diagnostic technique used to nonintrusively quantify various thermodynamic properties of a light-scattering gas. The backbone of FRS is the molecular filtering of Rayleigh scattered light. This concept was initially introduced by the atmospheric LIDAR community before being adopted within the aerospace research field in the early 1990s. Since then, FRS has matured into a versatile quantitative diagnostic tool and has found use in a variety of flow regimes ranging from sub- to supersonic speeds in both reacting and non-reacting environments. This adoption can be attributed to the wealth of information that can be obtained via FRS, including the gas density, pressure, temperature, velocity, species composition, or, in some cases, several of these properties at once. This article reviews the current state of FRS methodology in recovering such gas properties. As knowledge of the fundamentals of Rayleigh scattering and spectral light filtering is crucial to the design of an FRS experiment, we begin by briefly reviewing these areas. Subsequently, we conduct a survey of experimental design strategies, assumptions, and data reduction methods used to measure different gas properties using FRS. We conclude the review with a short discussion on quantification of experimental uncertainty and future trends in FRS.

Submitted to: *Meas. Sci. Technol.*

1. Introduction

Laser-based diagnostic techniques have long been used to nonintrusively quantify the thermodynamic properties of gases. Such techniques have been adopted across an array of scientific disciplines due to their ability to make measurements in environments unsuited for traditional probe-based techniques. Some laser-based diagnostic techniques can capture measurements across large regions, such as flow-planes or volumes, or measure thermodynamic variables and transport properties that are otherwise unmeasurable with intrusive techniques.

A wide range of laser-based diagnostic techniques can quantitatively characterize gaseous media. These include laser absorption spectroscopy (LAS), laser induced fluorescence (LIF), Rayleigh and Raman scattering, coherent anti-Stokes Raman spectroscopy (CARS), and femtosecond laser electronic excitation tagging (FLEET), just to name a few. If velocity is the primary measurand of interest, and the gas is able to be seeded with flow tracing particulates, particle image velocimetry (PIV) can also be implemented. Overviews of these techniques, and others, are found in references [1, 2, 3, 4, 5, 6, 7].

The laser-based diagnostic technique that is most appropriate for a particular experiment is governed by multiple factors. First and foremost, one must consider the environment in which the measurement will take place. In the study of gaseous flows, features of the flow that will influence the selection of a diagnostic technique include, but are not limited to, whether the flow is reacting or nonreacting, is sub- or supersonic, and whether the flow is in thermochemical equilibrium. One must also consider the desired thermodynamic property to be measured, the amount of optical access to the region of interest, and the equipment required to perform the measurement. A particular diagnostic technique is more attractive if it is both highly versatile and accessible. A technique's versatility is its ability to quantify different thermodynamic properties of a gas across a wide variety of flows with varying amounts of optical access. It is a distinct advantage if the technique can quantify multiple thermodynamic properties simultaneously and/or do so with as little optical access as possible. A technique's accessibility is how challenging it is to implement in practice—both in relation to the availability and cost of the equipment required to perform the measurement, and the amount of time it takes an "average" diagnostician to learn, implement, and acquire meaningful data with the technique. The focus of this article is the technique known as filtered Rayleigh scattering. FRS is of increasing interest within the nonintrusive diagnostic community because it is both highly versatile and increasingly accessible, which has led to its rapid development within the past decade. As will be gleaned from this review, the unique appeal of FRS is its ability to measure almost all of the major thermodynamic properties of a gas, without flow-seeding, in a wide variety of flows with relatively accessible laboratory grade lasers and detectors.

FRS is a variation of traditional Rayleigh scattering techniques. Broadly, the core of any Rayleigh scattering technique is to use a laser beam or two-dimensional laser

sheet to illuminate a region of interest and then image the light scattered from the gas atoms and molecules using a detector. In the traditional (unfiltered) Rayleigh scattering approach, the intensity of the scattered light is directly proportional to the scattering gas' number density [8]. This allows for quantitative measurement of density [9, 10, 11, 12, 13], mixture fraction [14, 15, 16, 17, 18, 19, 20, 21], or, if the gas' pressure is known, temperature can be recovered using the ideal gas law [22, 23, 24].

Rayleigh scattering has several advantages over other nonintrusive techniques. For example, unlike LIF, Rayleigh scattering is generated by illumination sources of all wavelengths. Because it does not require a fluorescing species to be present, there is no need to seed the flow with a fluorescent flow-tracer as is done in many LIF experiments. This allows Rayleigh scattering to be implemented in environments not conducive to flow-seeding. Additionally, because it is a molecular scattering technique, the difficulties in signal interpretation that sometimes arise in LIF experiments due to laser absorption or collisional quenching are also avoided with Rayleigh scattering [25]. Unfortunately, the relatively small scattering cross sections of gaseous atoms and molecules result in Rayleigh scattering having a signal intensity that is often much weaker than other sources of light scattering. For example, Mie scattering from particles and geometric scattering from surfaces and windows often obfuscates the Rayleigh signal.

Because the intensity of Rayleigh scattered light scales inversely proportional to the fourth power of the illuminating wavelength, one way to increase the intensity of the Rayleigh signal is to use an ultraviolet (UV) laser source. This comes with an added benefit of increasing the signal-to-noise ratio (SNR) because geometric scattered light does not scale at the same rate [26]. UV Rayleigh scattering has been successfully demonstrated in both sub- and supersonic flows [10, 27, 28]. However, this approach comes with a major drawback that has limited its uptake. UV laser sources, optics, windows, and detectors are, generally, not as accessible as similar equipment used in the visible light range. Additionally, UV detectors tend to be less sensitive and, in reacting flows, the Rayleigh signal can be interfered with by fluorescence from the combustion products.

Instead of performing experiments in the UV range, the most popular way to solve the background interference problem is to place a sharp-cutoff atomic or molecular absorption filter before the detector. This filter separates the Rayleigh scattering from other unwanted sources of scattered light. The addition of the filter makes the technique known as filtered Rayleigh scattering. In addition to attenuating background interference, the filter also makes the recorded signal intensity dependent upon the Doppler frequency shift of the Rayleigh scattered light, which can be exploited to measure the gas velocity. The ability to measure gas velocity gives FRS an advantage over PIV in situations where flow seeding is not possible. Additionally, the measurement error due to particle lag is avoided.

Since its first demonstration in the early 1990s [29, 30], FRS has proven to be broadly applicable across many flow regimes and is now a reliable diagnostic tool implemented by an increasing number of groups around the world. FRS has the unique

capability of being able to measure various thermodynamic properties of a gas, including temperature, pressure, density, velocity, and binary mixture composition. These measurements can be made independently or, in some cases, multiple thermodynamic properties can be measured at the same time. This review provides a detailed survey of experimental design strategies, assumptions, and data reduction methods required to make quantitative measurements of each of these properties with FRS.

Left out of this review is a discussion of interferometric Rayleigh scattering (IRS). Instead of using a molecular absorption filter as in FRS, IRS utilizes a Fabry-Pérot etalon to spectrally separate the narrowband geometric scattering from the thermally-broadened Rayleigh scattering. Though it is similar to FRS in many ways, the finer details of the experimental setup and signal interpretation of IRS are different enough that we consider it a separate technique. Interested readers are referred to [31, 32, 33, 34, 35] for a discussion of IRS.

This article is organized as follows. In Section 2, we give a brief overview of FRS scattering theory and FRS equipment. Subsequently, in Section 3, we discuss how to use FRS to obtain quantitative gas measurements and how to quantify uncertainty of these estimates. Finally, in Section 4, we discuss future trends in the application of FRS and conclude.

2. Brief review of filtered Rayleigh scattering theory and implementation

Rayleigh scattering takes place when an electromagnetic wave is elastically scattered by a particle whose effective diameter is less than one-tenth of the wavelength of the incident wave [36, 37]. In this review, Rayleigh scattering occurs in the context of an FRS experiment where laser light is scattered by the constituent atoms and molecules of a gaseous medium. In Section 2.1, we begin our discussion with a description of the typical FRS experimental arrangement and presentation of the equation for the radiant energy of the scattered light signal reaching the detector. The various terms of this equation and their functional dependencies are elaborated upon in order to give a clear picture of how this equation can be manipulated to measure thermodynamic gas properties. Subsequently, we discuss modeling Rayleigh scattered spectral lineshapes in Section 2.2 and typical FRS equipment, including a brief overview of molecular filtering, in Section 2.3.

2.1. Theory of the typical FRS Experiment

The primary components of a typical FRS experimental setup are a tunable narrow-linewidth laser (i.e., a bandwidth on the order of ten to a few hundred MHz), a molecular/atomic vapor notch filter, and a detector. Most commonly, the detector is a scientific camera with two-dimensional measurement capability. The governing equations presented in this section are valid for any type of laser, filter, and detector. However, there are many practical considerations that dictate the selection of equipment

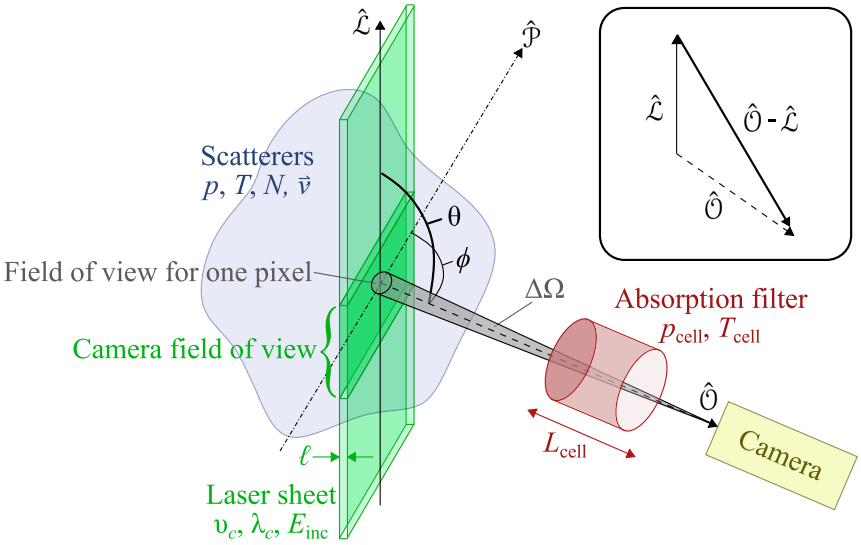

Figure 1: Schematic of a general FRS optical arrangement.

employed in an FRS experiment as discussed in Section 2.3.

A schematic depicting the arrangement of a generic FRS experiment is shown in figure 1. In this schematic, the incident laser light takes the form of a 2-D sheet that is propagating in the $\hat{\mathcal{L}}$ direction and is polarized in the $\hat{\mathcal{P}}$ direction. The sheet has a thickness ℓ, an incident energy E_{inc}, and a central frequency of ν_c. The laser sheet interacts with a volume of gaseous scatterers whose thermodynamic state (static pressure, p, static temperature, T, and molecular composition) and bulk velocity ($\vec{v}$) can either be completely or partially unknown. Light is scattered in the $\hat{\mathcal{O}}$ direction, which is at an angle ϕ from $\hat{\mathcal{P}}$ and at an angle θ from $\hat{\mathcal{L}}$. The scattered light then passes through an absorption filter. The vapor species used in the cell must have an absorption feature within the tunable wavelength range of the incident laser. Typically, there is only one absorbing species that is appropriate for a specific illuminating laser type. However, the filter length (L_{cell}), as well as the pressure (P_{cell}) and temperature (T_{cell}) of the vapor in the cell, can be manipulated to fine-tune the transmission profile for optimal performance as discussed in Section 2.3.2. Finally, the filtered light is collected by a detector over a solid angle $\Delta\Omega$.

The FRS signal, S, measured by the detector is linearly proportional to the total radiant energy that reaches the detector, E. This is written simply as,

$$S = AE + C, \tag{1}$$

where A is a constant that takes into account the various optical efficiencies and gain of the detector, and C is the zero offset of the detector. If the detector is two dimensional, Equation 1 (and each of the subsequently presented equations) is specific to each resolution element of the detector. For concision, we have omitted all spatial dependencies and pixel indices from the equations. The total radiant energy that reaches the detector, E, is equal to the sum of the radiant energy that passes through the filter

from all light scattering processes. This can be expressed as,

$$E = E_{R,\ filtered} + E_{b,\ filtered}, \tag{2}$$

where $E_{R,\ filtered}$ is the filtered radiant energy of the Rayleigh scattered light and $E_{b,\ filtered}$ is the filtered radiant energy of the background interference. The energy of the filtered Rayleigh scattered light, $E_{R,\ filtered}$, is equal to,

$$E_{R,\ filtered} = N\ell E_{\text{inc}}\Delta\Omega \sum_n \left[\chi_n \frac{\mathrm{d}\sigma}{\mathrm{d}\Omega}_n \int_{-\infty}^{+\infty} t(\nu)\mathcal{R}_n(\nu - \nu_c - \Delta\nu_D, \theta, T, p)\mathrm{d}\nu \right]. \tag{3}$$

In Equation 3, N is the total number density of the scattering gas mixture, ℓ is the laser sheet thickness (in the $\hat{\mathcal{O}}$ direction), E_{inc} is the incident laser energy, and $\Delta\Omega$ is the solid angle over which the sensor collects light. The summation in Equation 3 combines terms that are dependent on the properties of the individual species, n, in the scattering gas mixture, with each contribution weighted by its mole fraction, χ_n [38]. Within the summation, $\mathrm{d}\sigma/\mathrm{d}\Omega_n$ is the differential scattering cross section of species n. The differential Rayleigh scattering cross section is defined as the ratio of radiant energy intensity scattered in a given direction to the incident irradiance. $\mathrm{d}\sigma/\mathrm{d}\Omega_n$ is a function of the angle between the observation and polarization directions (ϕ), the central frequency of the incident laser light (ν_c), and the properties of the scattering gas. Expressions for the differential Rayleigh scattering cross sections for various polarization states of the laser source are given in [8]. Due to the dependence of the differential scattering cross section on the index of refraction, the intensity of the Rayleigh scattered light is dependent upon the molecular composition of the scattering gas. This dependence can be exploited to perform mixture composition measurements, which are discussed further in Section 3.2.

The integral in Equation 3 is the convolution of the Rayleigh scattered light spectrum from species n, $\mathcal{R}_n$, with the transmission spectrum of the absorption filter, $t(\nu)$. Both profiles are normalized prior to the convolution. This integral describes the fraction of light scattered by species n that reaches the detector. If no filter is present, the integral is equal to one and Equation 3 represents an unfiltered Rayleigh scattering experiment. When a filter is used, the Rayleigh scattered light is spectrally modified. Even though the precise Doppler-shifted Rayleigh lineshape may not be resolved in an FRS experiment, the integral term in Equation 3 retains a dependency on $\mathcal{R}_n$ which enables FRS to measure more flow parameters than an unfiltered Rayleigh scattering experiment.

Elaborating further on the terms in the convolution integral in Equation 3, t is a function of frequency (ν), the pressure and temperature of the filter gas (P_{cell} and T_{cell}), and the optical length of the filter (L_{cell}). The angle between the scattered light and filter face also weakly influences the transmission (through small changes in optical path length through the filter), however, this dependence is typically neglected. $\mathcal{R}_n$ is itself a

convolution of the laser lineshape, $l(\nu)$, and the unfiltered Rayleigh-Brillouin lineshape, r_n, and can be expressed as,

$$\mathcal{R}_n = \int_{-\infty}^{+\infty} l(\nu - \nu') r_n(\nu', \theta, T, p) d\nu'. \tag{4}$$

The Rayleigh-Brillouin lineshape, r_n, depends upon the observation angle (θ), the thermodynamic properties of the gas (T, p), as well as species-specific transport properties. Hence, in a multispecies mixture, light scattered from each species will have a different lineshape. The models used for predicting $r(n)$ are discussed further in Section 2.2. Because a narrow-linewidth laser is employed in FRS, it is often assumed that the laser profile is monochromatic. In this case, $l(\nu)$ reduces to a point mass distribution at the laser's central frequency, ν_c, and $\mathcal{R}_n = r_n$. Though this assumption is somewhat common, it can introduce varying amounts of systematic uncertainty in the FRS property measurement depending upon the actual linewidth and spectral purity of the laser [39, 40]. The ramifications of the spectral purity of the incident light source are discussed further in Section 2.3.1. Finally, if the gas has a bulk velocity, $\vec{v}$, $\mathcal{R}_n$ will be Doppler shifted in the $\hat{\mathcal{O}} - \hat{\mathcal{L}}$ direction prior to convolution with the filter's transmission profile, $t(\nu)$ as expressed below:

$$\Delta\nu_D(\theta, \vec{v}) = \frac{\nu_c \vec{v}}{c} \bullet \left(\hat{\mathcal{O}} - \hat{\mathcal{L}}\right), \tag{5}$$

where c is the speed of light. The Doppler shift of the signal can be exploited to measure the velocity, as discussed in Section 3.4.

The other term in Equation 2, $E_{b,\ filtered}$ can be written as the sum of the background interference from the geometric and Mie scattering components,

$$E_{b,\ filtered} = E_{geometric,\ filtered} + E_{Mie,\ filtered}. \tag{6}$$

Ideally, the filter would completely attenuate all unwanted scattering and $E_{b,\ filtered}$, would be identically zero. However, in practice, some background light will always reach the detector. Thus, it is important to understand the two primary sources of background interference and how they can be minimized.

The geometric component of background scattering generally emanates from stationary objects, thus it is not Doppler shifted. Additionally, its lineshape is not broadened and is typically assumed to be equal to that of the illuminating laser, $l(\nu)$. This is shown in Equation 7, where the energy of the geometric scattering component is equal to the product of the geometric scattering cross section, β, the incident laser energy E_{inc}, and the convolution of the laser's spectral profile with the filter's transmission profile [41].

$$E_{geometric,\ filtered} = \beta E_{inc} \int_{-\infty}^{+\infty} t(\nu) l(\nu - \nu_c) d\nu, \tag{7}$$

The inherent complexity of Mie scattering theory means that the Mie scattered energy reaching the detector, $E_{Mie,\ filtered}$, is typically not calculated with a physics-based model. In experiments with infrequent interference from Mie scattering, the affected data can either be removed from the data set or, if the influence from Mie scattering is confined to a small region in a large 2-D image, locally filtered out with image post-processing routines. In cases where this is not possible, other strategies must be adopted since Mie scattering interference can introduce bias errors in FRS property measurements. Recently Boyda et al. introduced a method to account for Mie scattering by estimating its spectrum as a normal distribution with a width determined by the turbulence intensity of the flow [42, 43].

Figure 2 schematically depicts the basic principle of FRS. Figure 2(a) shows Rayleigh scattering without the use of an absorption filter. The narrow spectrum of the incident laser light is plotted in blue. The spectrum of the unfiltered Rayleigh scattered light, plotted in black, is Doppler shifted with respect to the central laser frequency due to bulk fluid motion. The magnitude and direction of this Doppler shift is calculated with Equation 5. Figure 2(a) also shows that the spectral profile of the Rayleigh scattered light is thermally broadened with respect to the narrowband light source. Because the thermal velocity distribution of the gas changes with temperature, the width of the Rayleigh scattered spectrum is a function of temperature while its lineshape has both temperature and pressure dependencies. The radiant energy of the Rayleigh scattered light is equal to the integral of its lineshape over all frequencies (purple shaded region) and, for a single species gas, is directly proportional to the gas' number density. For a gas mixture the Rayleigh scattered signal is proportional to the total gas number density and the mole-fraction-weighted scattering cross sections of the mixture components. As specified in Equation 2, the recorded signal is the sum of contributions from the Rayleigh scattered light and that of any background scattering. Only geometric scattering is depicted here (blue shaded region). If Mie scattering existed, its contribution would be Doppler-shifted the same amount as the Rayleigh contribution, but its spectral width would be much narrower [43].

Figure 2(b) is similar to Figure 2(a) but now a filter is used. In this figure, the incident laser light is tuned such that its entire lineshape (blue curve) falls in the center of a strong absorption line (red curve). Thus, the background geometric scattering is attenuated. Like the previous example, the unfiltered Rayleigh scattering lineshape (black curve) is Doppler shifted and thermally broadened. However, some of the Rayleigh scattered light is absorbed as it passes through the filter and the measurement is proportional to the integral of the filtered Rayleigh scattering lineshape (green shaded region). From this figure one can glean the importance of choosing a sharp absorption feature that is both wide enough to remove geometric scattering and narrow enough that it does not overly attenuate the Rayleigh scattered signal.

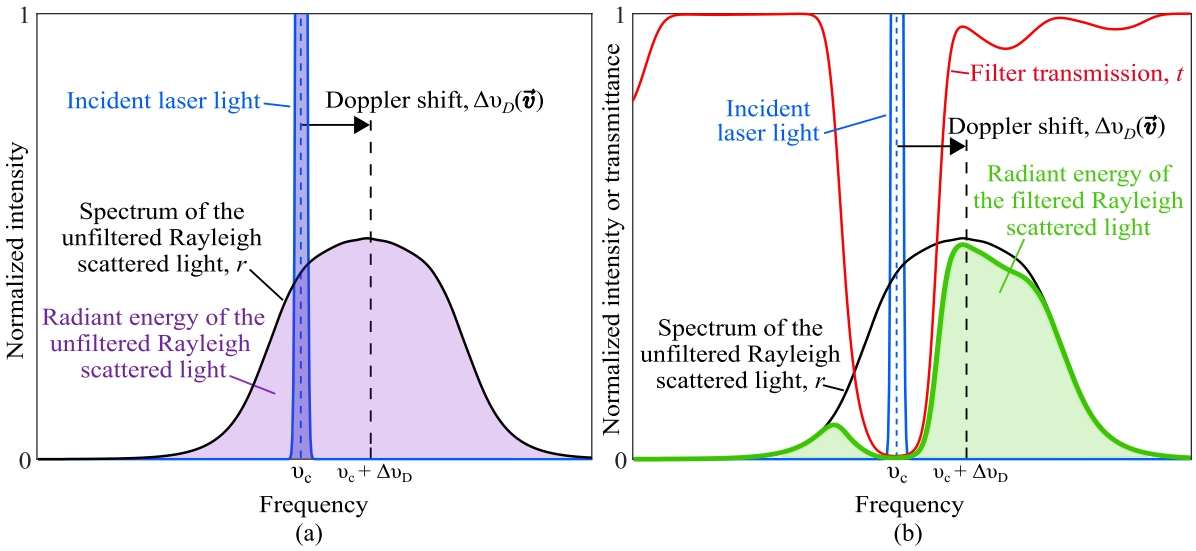

Figure 2: Simulated spectra that demonstrate (a) unfiltered Rayleigh scattering; (b) filtered Rayleigh scattering.

2.2. Modeling the spectral lineshape

Due to the thermal motion and internal degrees of freedom of the gaseous atoms and molecules comprising the scattering medium, the scattered light develops a spectral profile. This spectrum contains contributions across a wide frequency range from both the elastic Rayleigh scattering process and the inelastic Raman scattering process as illustrated in Figure 3(a). Since most detectors integrate over a wide range of optical frequencies, it is important to understand the various spectral components that contribute to the recorded signal and their relative intensities. While it is typically impossible to completely separate inelastic Raman scattering from the Rayleigh signal, its contributions to the integrated light intensity are small and, therefore, typically ignored when modeling. It is estimated that the contribution to the integrated intensity is 0.1% for vibrational Raman [41], 1% for the Raman Q-branch [8] and, in air, approximately 2.5% for the rotational Stokes/anti-Stokes Raman bands [41].

Modeling the spectral lineshape of the Rayleigh scattered light, r, is central to many applications of FRS. Typically, the lineshape model is a function of a nondimensional frequency, x, and a nondimensional "y-parameter" denoted y [44], which are defined as follows:

$$x = \frac{(\nu - \nu_c)\lambda_c}{2sin(\theta/2)} \left(\frac{m}{2k_bT}\right)^{1/2}, \tag{8}$$

$$y = \frac{\lambda_c p}{4\pi\eta sin(\theta/2)} \left(\frac{m}{2k_bT}\right)^{1/2}, \tag{9}$$

where λ_c is the incident laser's central wavelength, η is the shear viscosity, m is the scatterer's mass, and k_b is the Boltzmann constant. Physically, the y-parameter is the ratio of the scattering wavelength to the molecular mean free path and determines in

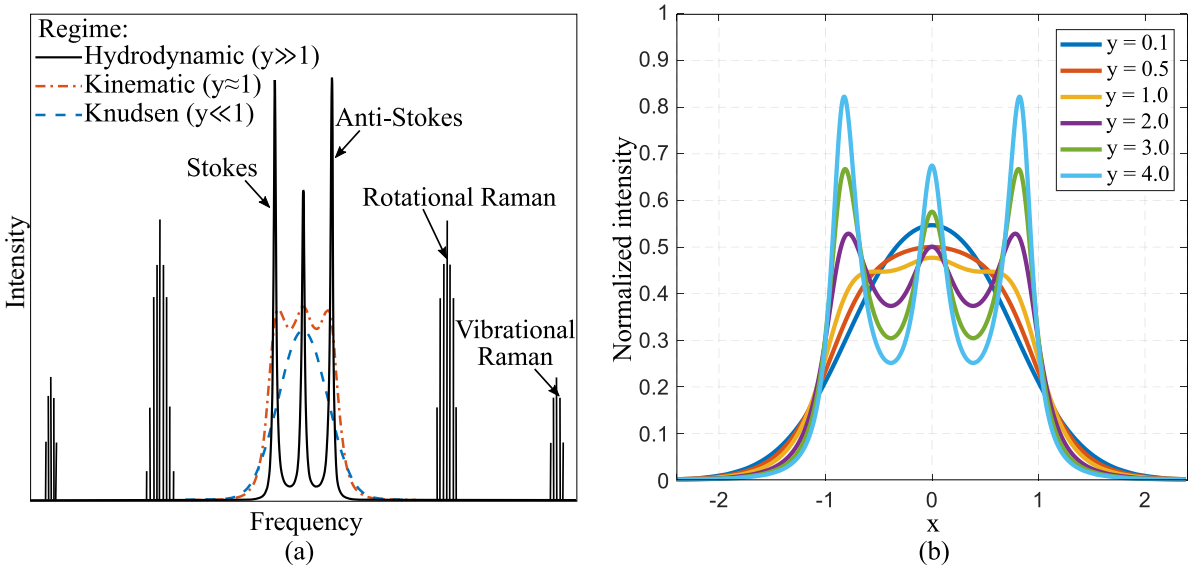

Figure 3: (a) Illustrative spectrum (frequency and intensity not to scale) showing the approximate relationship between the Rayleigh and Raman scattering components. Adapted from Ref. [45]. (b) Normalized Rayleigh scattered lineshapes calculated with the Tenti S6 model for various y-parameters.

which of three defined regimes the scattering exists. In one extreme is the Knudsen regime, where $y \ll 1$. In the Knudsen regime, the gaseous scatterers have a very low density, meaning that the the mean free path is much larger than the scattering wavelength. In this case, the resulting lineshape, r, is simply a Gaussian curve corresponding to the Maxwellian velocity distribution of the scatterers. In the opposite extreme lies the hydrodynamic regime, occurring where $y \gg 1$. In this regime, there is a very high density of gaseous scatterers and the gas can be considered a continuum with a mean free path significantly smaller than the scattering wavelength. When approaching the hydrodynamic limit, the spectral profile of the scattered light is characterized by three distinct Lorentzian-shaped peaks—one peak centered about the incident wavelength and two symmetrically displaced sidebands whose frequency shift is determined by the speed of sound in the gas [8].

Between these two limiting regimes exists the kinetic regime where the mean free path is on the order of the wavelength of the incident laser light, i.e., $0.1 \lesssim y \lesssim 4$. The modeling of spectra in the kinetic regime has attracted particular attention in literature because light scattering occurring near standard atmospheric conditions exists within this regime. The model that is generally accepted to produce the most accurate lineshapes within the kinetic regime is the s6 model developed by Tenti et al. [44] in 1974, which is still widely used today. In addition to the y-parameter, the s6 model depends on additional species-specific transport properties. Figure 3(b) plots example lineshapes against the nondimensional frequency x. These lineshapes are calculated with the Tenti s6 model for a range of y-parameters.

Though the Tenti s6 model assumes a single species gas, and does not take into

account the Raman Q-branch, it has been proven to accurately reproduce measured spectra for a wide variety of molecular species (e.g., O_2, N_2 and CO_2), as well as mixtures such as air [46, 47, 48]. There has been some effort to derive kinetic models that explicitly account for multiple species in the model formulation; however, these more complicated models have not gained considerable popularity because they have only been shown to be accurate for noble gas mixtures [46, 49]. Additionally, McManus et al. [38] have shown that the FRS signals of gas mixtures can be accurately predicted when the s6 model is used to calculate the spectra of the individual mixture components and the mixture-weighted formulation of Equation 3 is used to determine the total FRS signal. They demonstrated this for binary mixtures of CH_4/N_2, H_2/N_2 and CO_2/N_2 over a range of temperatures between 300 and $1400K$. They also measured FRS signals in H_2/air and CH_4/air flames that agree well with model predictions. From this they infer that the s6 model likely accurately predicts the spectra of the combustion products for the atmospheric pressure flames they investigated. While the s6 model has been proven to work well for several use cases outside of the original framework of its derivation, Doll et al. [50] found a model-induced bias in a turbulent jet experiment. They hypothesize that the bias arose because the s6 model does not contain contributions from inelastic scattering and because it requires knowledge of the bulk viscosity, which is notoriously difficult to accurately quantify. To remedy this bias they introduced an analytical lineshape model which they calibrated to the conditions of their turbulent jet experiment.

Other kinetic models have been developed in addition to the popular s6 model. A kinetic model developed by Pan et al. [51], the Pan s7 model, uses a similar linearization as the Tenti s6 model but retains seven moments (instead of six) in the collision integral. Another physical model developed by Zheng linearizes a modified equation set while retaining nine moments and is able to calculate both polarized and depolarized Rayleigh-Brillouin spectra [52].

One drawback of physics-based spectra models models is that they often impose a high computational burden. While individual evaluations of the models may be quick, when evaluated iteratively as part of optimization or flow parameter estimation routines, they can be a computational bottleneck [53, 54, 55, 56]. Such issues have motivated a small number of methods to quickly calculate Rayleigh spectra by approximating the s6 model. While the Tenti s6 model has five input parameters, most approximation approaches only incorporate y as it has the largest impact on the lineshape. For example, Witschas et al. model the Rayleigh spectra as a central Gaussian curve representing the Rayleigh peak with two superimposed shifted Gaussians to represent the Brillouin doublet. The heights and widths of the three Gaussian curves are fit as a function of y using empirical data [57]. This approximation was validated for atmospheric conditions with y between about 0 and 1. A similar approach is taken by Ma et al. who instead consider a superposition of three Voigt lineshapes and show that this approximation works well for values of y up to about four [58].

Modeling the spectra in a different way, Binietoglou et al. propose and validate

a polynomial-fit principal components regression [56]. Their model uses a library of precomputed Rayleigh spectra to learn the principal components of the data and then relate linear combinations of these principal components to the lineshape through polynomial regression. This approach was validated for N_2 with a value of y up to about 2. This principal-components-based approach was extended by Hunt et al. [59] to allow modeling of the Rayleigh spectra using all parameters of the s6 and s7 models. The approach uses principal components analysis (PCA) to compress a library of precomputed spectra and then learns the relation between linear combinations of these principal components and the Rayleigh spectra using support vector regression (SVR), a machine learning technique. This approach was validated for both coherent and spontaneous Rayleigh spectra over a wide range of the five input parameters to the s6 model: y-parameter, Eucken factor, internal relaxation number, internal specific heat, and translational specific heat. The compression achieved by PCA combined with the flexible and sparse solutions found by SVR create a highly accurate and extremely computationally efficient approximator that calculates lineshapes approximately 3 orders of magnitude faster than the Tenti s6 model.

2.3. FRS equipment and practical implementation

In this section we discuss topics relevant to the selection of each major component of an FRS system: the laser, the filter, and the detector. Since every experiment and situation is unique, the topics covered herein will not be all-encompassing. Instead, this section should be interpreted as a brief introduction to the some of the most common equipment utilized by FRS practitioners and the relevant tradeoffs one must consider.

2.3.1. Laser FRS requires a tunable-frequency narrow-linewidth laser whose linewidth is narrower than the targeted absorption feature of the vapor notch filter. As mentioned previously, Rayleigh scattering is generated by all wavelengths of light. Thus, as long as there exists a vapor species that produces a suitable absorption feature within the tunable range of a narrow-linewidth laser, any wavelength illumination source can be used. However, the FRS community has generally coalesced to a preferred illumination wavelength for FRS experiments: 532 nm. At this wavelength, molecular iodine serves as the vapor notch filter. Additional laser/filter pairs have been used for FRS, and are discussed in the following subsection. 532 nm is the preferred illumination wavelength for FRS because of the increased access to, and affordability of, the required system components when compared to other wavelengths. For this reason, this subsection will only discuss the specifics of the types of lasers used for 532 nm illumination.

The first applications of FRS by Miles et al. [26, 29, 60] utilized an injection-seeded frequency-doubled Nd:YAG laser for pulsed illumination at 532 nm with 7 ns pulse duration. Their laser had a Fourier-transform-limited linewidth of 60 MHz with energies of 330 mJ per pulse. Because of the ability to obtain high pulse energies (e.g., up to 850 mJ per pulse [61]) with linewidths around $50-150$ MHz, the injection-seeded

Nd:YAG became ubiquitous in early FRS work, and is still commonly used today.

However, many researchers using frequency-doubled injection-seeded Nd:YAG lasers for FRS have reported stray light attenuation levels orders of magnitude less than the theoretically predicted values [19, 62, 63, 64]. The suspected cause of this underperformance is that, due to mode competition inherent to the injection-seeding process, the spectral profile of the output beam consists of a narrow peak superimposed onto a broadband pedestal [65]. In an FRS experiment, the background light scattered from the broadband pedestal could fall outside of the targeted absorption feature and remain unfiltered, decreasing the SNR of the measurement. Patton and Sutton [40] were the first to investigate this issue systematically and found that if 0.1% of the laser's energy is in the broadband pedestal, then the realizable attenuation of the iodine filter can decrease by more than six orders of magnitude. Sutton and Patton [65] subsequently demonstrated that the broadband pedestal can be attenuated by using a tunable Fabry-Pérot etalon as a ultra-narrowband spectral filter. This greatly increased the spectral purity of the output laser beam, resulting in a two orders of magnitude increase in the achievable attenuation of their iodine filter. Separately, Forkey et. al [66] have documented a 100 MHz spatial frequency variation across the beam of an injection-seeded Nd:YAG laser, which introduced a significant bias error in FRS velocity measurements [39].

Citing these issues, some researchers have used continuous wave (CW) lasers, like diode-pumped solid state frequency-doubled Nd:YVO_4 lasers, to provide 532 nm illumination with linewidths less than 5 MHz at powers up to 18 W [42, 43, 50, 67, 68, 69, 70]. These spectrally pure illumination sources have enabled measurements in challenging internal flow environments with a large amount of background scattering. However, FRS experiments utilizing CW lasers are currently limited to time-averaged measurements due to the relatively long detector exposure times required to achieve a high SNR measurement. Recent work [71] suggests that long pulse lasers might be able to provide spectral purities similar to that of CW lasers while also providing pulse energies high enough to enable time-resolved multiproperty FRS measurements. To date, these lasers have not been implemented in an FRS experiment.

2.3.2. Absorption Filter Spectral light filtering attempts to isolate the Rayleigh scattered light from background interference. As seen in Section 2.1, filtering also modifies the recorded signal in such a way that allows for the quantification of gas temperature and velocity. In this section, we briefly discuss a few of the most commonly used filter choices.

In its most basic form, a filter cell is a cylinder with flat, optical-quality windows at each end. The gas species inside the cell determines the central wavelengths of the absorption lines. The cell length, along with the pressure and temperature of the gas in the cell, can be varied to adjust the width and depth of these absorption lines. Because geometric scattering has a spectral profile that is not broadened or shifted from its source, the filter must have an absorption feature within the tunable wavelength range

of the incident laser.

By far the most common filter/laser pairing is a molecular iodine filter and an Nd:YAG laser (532 nm). Iodine can also be used as the absorbing species for a CW argon-ion laser (514.5 nm) illumination source, as was demonstrated by Komine et al. in their initial Doppler global velocimetry measurements [72], and utilized for FRS by Reeder et al. [73, 74]. As mentioned previously, the intensity of Rayleigh scattered light scales with $1/\lambda^4$, so the strength of the Rayleigh scattered signal greatly increases when using a UV illumination source [8]. This has motivated the use of a mercury vapor cell paired with 254 nm illumination sources, either a frequency-tripled titanium:sapphire (Ti:Al2O3) laser [75] or a frequency-tripled single-longitudinal-mode alexandrite laser [76]. For similar reasons, Golz & Andresen [77] paired an atomic iron vapor filter with a KrF excimer laser (248 nm). The previously mentioned lasers are all solid-state lasers, but diode lasers have also been utilized. These lasers have a lower intensity output, and therefore, the resulting Rayleigh signal is lower. However, diode lasers are less expensive and have rapid tuning capabilities that make them ideal for frequency-modulated FRS techniques. Mach and Varghese [78] paired a GaAlAs diode laser emitting at around 780 nm and a rubidium vapor filter to acquire velocity measurements of a supersonic jet. Additional filter/laser pairs have been used for LIDAR and other diagnostic techniques and could potentially be used for FRS, but haven't been demonstrated yet [79, 80, 81].

While only one absorbing gas species is typically appropriate for a given laser type, the conditions of the vapor in the filter can be manipulated to fine-tune the transmission profile for optimal performance. Ideally, there exists a strong absorption line (i.e., with a low transmittance) to block background scattering with high transmittance in its immediate vicinity to prevent attenuation of the Rayleigh scattered signal [8]. This generally implies that the chosen absorption line should be spectrally narrow and separated from other absorption lines. In addition, it is also desirable to have abrupt transitions from absorption to transmission, i.e., a sharp cutoff, to provide high spectral resolution and measurement accuracy [82]. The addition of nonabsorbing species, such as nitrogen, to the filter cell results in a more gradual transition and wider line width [41]. Thus, one must be careful to ensure the cell is free of gas contaminates, unless the nonabsorbing gases are added purposefully to fine tune the spectral characteristics of the filter cell.

The filter cell length (L_{cell}), gas pressure (P_{cell}), and gas temperature (T_{cell}) can be adjusted to achieve the desired characteristics mentioned above. As an example, consider the most common filter choice: an iodine vapor cell. Figures 4(a) and (b) show different iodine transmission profiles calculated with the model developed by Forkey et al. [83]. Generally, increasing the cell length or the density of the absorption species (shown in Figure 4(b) as a change in cell temperature for a cell of constant length and pressure) broadens and strengthens the absorption line. Additionally, as the vapor density increases, so too does continuum absorption, leading to an overall decrease in transmission.

Forkey et al. compared their iodine transmission model to experimental data and

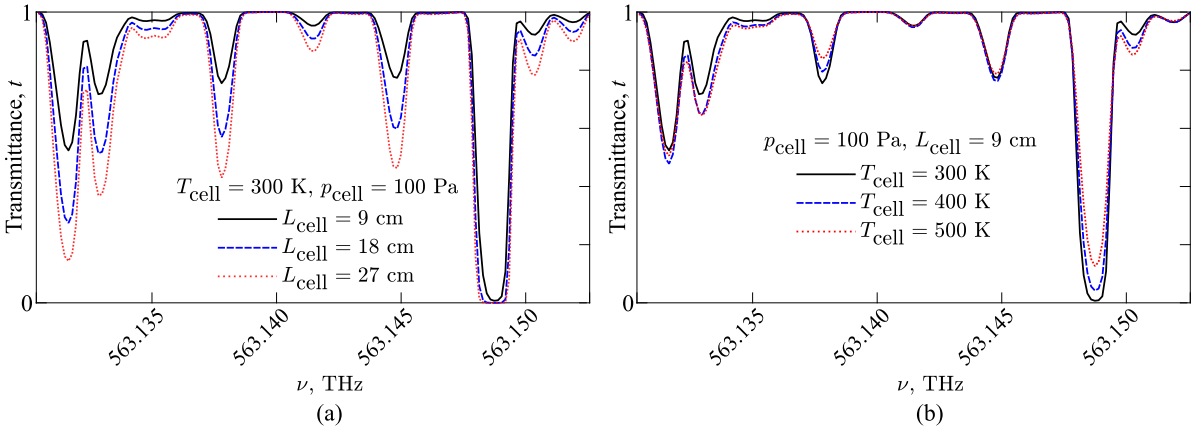

Figure 4: Iodine transmission spectra for: (a) different cell lengths at constant density; (b) different cell density at constant cell length.

found that the model predicts the presence of all observed absorption lines in the 532 nm region accessible to tunable Nd:YAG lasers. They found that for optically thick lines the model predicts linewidths within ±2%, maximum slopes to ±6% and optical depths to ±10% accuracy. Due to these uncertainties, many researchers [64, 67, 82, 84, 85, 86], including Forkey [87], choose to experimentally characterize the filter's transmission profile to achieve greater accuracy for the resulting FRS property measurements. Nevertheless, Forkey et al.'s model remains invaluable to FRS experiment design.

To compare transmission profiles of filters for different absorbing species, Figure 5 shows example transmission spectra of a 5-cm long mercury vapor cell for the frequency range accessible by UV lasers near 254 nm [75]. Three different spectra are shown, corresponding to different cell pressures, and were calculated using the model developed by Finkelstein [88].

2.3.3. Detector In a typical FRS experiment, the detector can be either a scientific camera that acquires a 2-D image of the FRS signal or a device such as a photodiode or photomultiplier tube that acquires a point-measurement. When acquiring 2-D FRS images, there are generally two camera types that can be used, charge coupled device (CCD) cameras and complementary metal oxide semiconductor (CMOS) cameras. Both of these camera types can be intensified or unintensified. Additionally, unintensified cameras can be coupled to gated intensified relay optics systems. Because Rayleigh scattering is a relatively weak scattering process, it is important that the chosen camera have a high quantum efficiency with low readout noise. Other important characteristics to consider when selecting a camera are the linearity and uniformity of the intensity response across the sensor, the repeatability and accuracy of the shutter, and the amount of image lag (a.k.a "ghosting") between successive frames. Hain et al. [89] provided a comparison of the performance of CCD, CMOS, and intensified cameras from the perspective of an experimental fluid dynamicist, however the specific hardware detailed therein is now several generations old. Manin et al. [90] provided a more recent

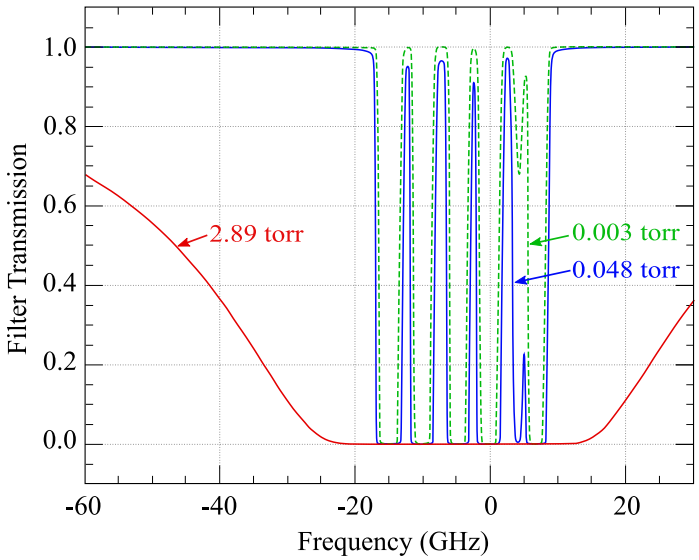

Figure 5: Mercury transmission spectrum for a 5-cm long filter cell at 3 different cell pressures. Adapted from Yalin and Miles [75].

performance comparison of two commercially available high-speed CMOS cameras. However, because scientific camera technology is constantly evolving, most detailed hardware comparisons quickly become out of date. Thus, it is incumbent upon the diagnostician to remain apprised of the latest technological advancements. For this reason only a few salient points are discussed herein.

CCD cameras have traditionally been used for quantitative FRS measurements due to their highly linear response across the entire pixel array [41]. Early FRS work made use of the signal gain capability offered by intensified CCD (ICCD) cameras due to the relatively weak signal produced by the Rayleigh scattering process [26, 63, 64, 91, 92]. Improvements in laser and detector technology have enabled the use of modern unintensified CCDs for FRS [61, 93, 94], which have much less noise than ICCDs. Another option demonstrated in FRS experiments is the electron-multiplied CCD (EMCCD) [67, 95, 96]. EMCCDs have the signal gain capabilities of an ICCD but make use of on-chip multiplication instead of traditional image intensification, resulting in higher quantum efficiencies and spatial resolution.

With the rapid development of scientific grade CMOS cameras, they are quickly replacing CCD cameras in many fluid dynamics applications like PIV, where CCD cameras have been almost completely phased out. The main benefit of CMOS cameras is that their analog-to-digital conversion happens in parallel for all pixels across the sensor array, so they can achieve much higher frame rates than CCD cameras, opening up the possibility of high-speed, time-resolved, FRS measurements. However, the previous generation of CMOS detectors were known to have an independent response for each pixel, potentially leading to spatial nonuniformity across the sensor [97]. Though this nonuniformity was thought to be small, Papageorge et al. [98] demonstrated a large spatial nonuniformity related to the temporal dependence of the CMOS detector in

response to ns-pulsed illumination. Nevertheless, they were able to obtain accurate measurements after performing a pixel-by-pixel calibration to correct for the nonuniform response. CMOS camera technology has rapidly matured over the past decade with major improvements in image noise reduction, linearity, and uniformity across the sensor. In fact, it is now generally accepted that modern CMOS cameras are equally as suitable as their CCD counterparts for many scientific applications [90, 99]. CMOS cameras have been used for FRS measurements by Boyda et al. [43] and will likely continue to be adopted as scientific CMOS cameras continue to develop and high speed FRS continues to be pursued.

3. Quantitative gas property measurements with FRS

The intensity of Rayleigh scattered light is a function of many variables, including those related to the laser, optical system, and flow (see Equation 3). In general, many of the optical system variables are known or can be eliminated by calibration and/or normalization. This typically leaves only the flow thermodynamic properties and velocity as unknowns. In order to quantify flow properties with FRS, one must: a) reduce the number of unknowns to a single flow property, or b) design the experiment to quantify multiple flow properties at once. As reviewed in the following subsections, both of these approaches have been demonstrated in the literature.

3.1. Temperature

One of the most common single-property FRS measurements is the measurement of static temperature. Early work by Hoffman et al. [63] made two-dimensional FRS measurements of static temperature in a sooting methane/air flame. They accomplished this by experimentally calibrating an analytical model of the FRS signal intensity in a separate, nonsooting, flame whose temperature distribution was initially measured with unfiltered Rayleigh scattering. Because Hoffman et al.'s FRS thermometry method required calibration with unfiltered Rayleigh scattering measurements, it is not generalizable to other FRS experiments.

Elliot et al. [100] developed the preferred technique for performing single-property static temperature measurements with FRS. This technique involves normalizing the FRS signal intensity, S, by a previously measured reference signal, S_{ref}. The FRS reference signal is recorded at a condition where the complete thermodynamic state and composition of the gas is known. This is typically quiescent air. If the same experimental setup is used to measure S and S_{ref}, and the background intensity is subtracted from both signals, then the signal intensity ratio, S/S_{ref}, can be written in the form of Equation 10. Note that the ideal gas law, $p = Nk_bT$, has been substituted into this form of the equation and a single scattering gas species is assumed.

$$\frac{S}{S_{ref}} = \frac{T_{ref}}{T}\frac{p}{p_{ref}}\frac{\frac{\mathrm{d}\sigma}{\mathrm{d}\Omega}\int_{-\infty}^{+\infty} t(\nu)\mathcal{R}(\nu-\nu_c-\Delta\nu_D,\theta,T,p)\mathrm{d}\nu}{\frac{\mathrm{d}\sigma}{\mathrm{d}\Omega}_{ref}\int_{-\infty}^{+\infty} t(\nu)\mathcal{R}(\nu-\nu_c-\Delta\nu_D,\theta,T_{ref},p_{ref})\mathrm{d}\nu} \tag{10}$$

To solve for T, the other flow properties in Equation 10 must be known, such as the gas pressure and flow velocity (i.e., Doppler shift). Equation 10's dependence on flow velocity is negated if the flow is stagnant or if the detector is positioned so that the Doppler shift is sensitive to a negligibly small component of velocity. If this is not possible, simultaneous particle image velocimetry (PIV) and FRS measurements can be performed [101], as first demonstrated by Most and Leipertz [102]. Additional thermodynamic properties of the scattering gas must be known to calculate the differential scattering cross section. If not enough information is known, one can consider multiproperty measurements or, if the gas composition is known, make the simplifying assumption that the differential scattering cross section is solely a function of temperature.

The gas temperature, T, is the only remaining unknown term in Equation 10 after the other flow properties are determined through prior knowledge, simultaneous measurement, or justifiable assumptions. Temperature dependence appears in the T_{ref}/T term, as an input to the lineshape $\mathcal{R}$ (both explicitly and implicitly through a variety of transport properties), and, in some cases, in the modeling of $\frac{\mathrm{d}\sigma}{\mathrm{d}\Omega}$. To recover the gas temperature, the right hand side of Eq. 10 is iteratively evaluated to find a value for T such that the result matches the measured S/S_{ref}. Often, a precomputed calibration curve such as Figure 6 is used. This example shows that the signal intensity ratio decreases with increasing temperature. As highlighted by Boguszko and Elliot [41], it is not guaranteed that this decrease is monotonic, thus T may not be uniquely determined. However, with proper pre-experiment modeling of the filter and experimental environment, a central laser frequency can typically be found that ensures the calibration curve is not multivalued.

3.1.1. Measurements in Flames As discussed previously, the application of the signal-ratio technique for FRS thermometry assumes that the differential scattering cross section and the lineshape $\mathcal{R}$ are known across the measurement region. This is a reasonable assumption in a single-species gas or a nonreacting mixture of gases, but is challenging to justify in flames where the flow is reacting and the composition of the gas is a spatially varying mixture of reactants, intermediates, and products. Nevertheless, FRS thermometry is often applied in flames by tailoring experiments to limit the variation of the differential scattering cross section in the flame. The lineshape term, $\mathcal{R}$, will also be different for each species in the combustion products, but this fact is often neglected in the literature and could be the source of some of the reported measurement error.

In early FRS flame temperature experiments, fuel and air were typically premixed prior to encountering the flame. In premixed flames, it is often assumed that the gas composition does not vary spatially. Some have made an additional simplifying assumption that the differential scattering cross section can be approximated as that of nitrogen, since nitrogen is generally the dominant species in the flame. This assumption is most accurate in premixed methane/air flames and has also been utilized in unfiltered

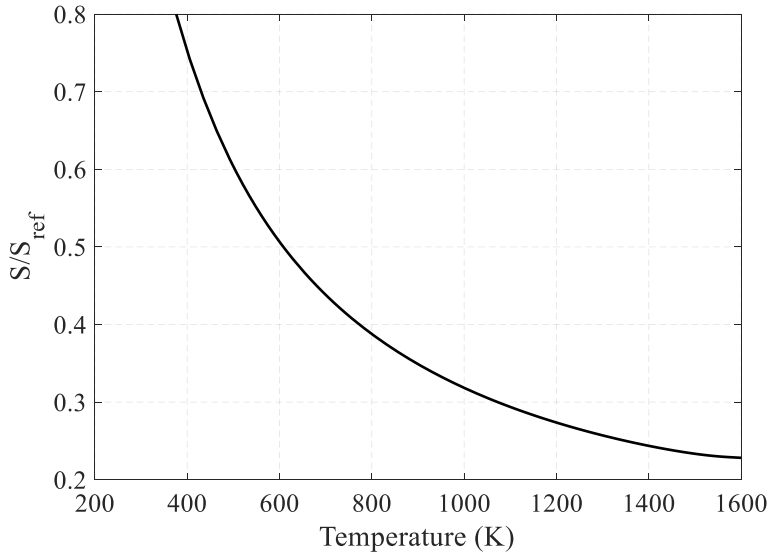

Figure 6: Analytical ratio of FRS signal intensity versus temperature. In this example, the scattering gas is a simulated stoichiometric methane/air flame where the mixture-averaged reaction products are used to calculate the FRS signal in the flame. Room temperature air is used as the reference condition. The incident laser frequency is 563.149 THz, and the iodine filter conditions are $P_{cell} = 100$ Pa, $T_{cell} = 300$ K, $L_{cell} = 9$ cm.

Rayleigh scattering experiments [22, 23, 24, 103]. Namer and Schefer [104] showed that the variation in differential scattering cross section between the reactants, intermediates, and products in certain premixed methane flames can be as low as 2%-4% and is very close to that of nitrogen. Using this assumption, Elliot et al. [84, 100] made temperature measurements in premixed methane/air and hydrogen/air flames that were accurate to within 4% and 8.5%, respectively. However, a significant portion of the measurement uncertainty could be attributed to the assumption of a nitrogen scattering cross section.

Zetterberg et al. [76] used a single-longitudinal-mode alexandrite laser coupled with a mercury vapor filter to make static temperature measurements in sooting premixed and diffusion methane/air flames. They too used the pure nitrogen assumption, but only for the particle mass term in the calculation of $\mathcal{R}$. They calculate the differential scattering cross section of the flame as a mixture-weighted average of the methane/air flame species predicted by an adiabatic flame calculation for the premixed flame, and use independent experimental species concentration measurements for the calculation of the differential scattering cross section in the diffusion flame. This approach led to temperature measurements in both flames that were consistent with thermocouple data.

More recently, Li et al. [105] performed FRS thermometry using the same simplifying assumptions of Elliot et al. [84, 100] in confined premixed methane/air flames. Their measurements were within 2.5% of thermocouple measurements made at the centerline of the flame for various equivalence ratios. As an example of the power of this thermometry technique, Figure 7 displays a collection of instantaneous temperature profiles of the swirling flame collected by Li et al. at a range of lean equivalence

ratios that show the temperature and cross-sectional area of the flame increasing with equivalence ratio.

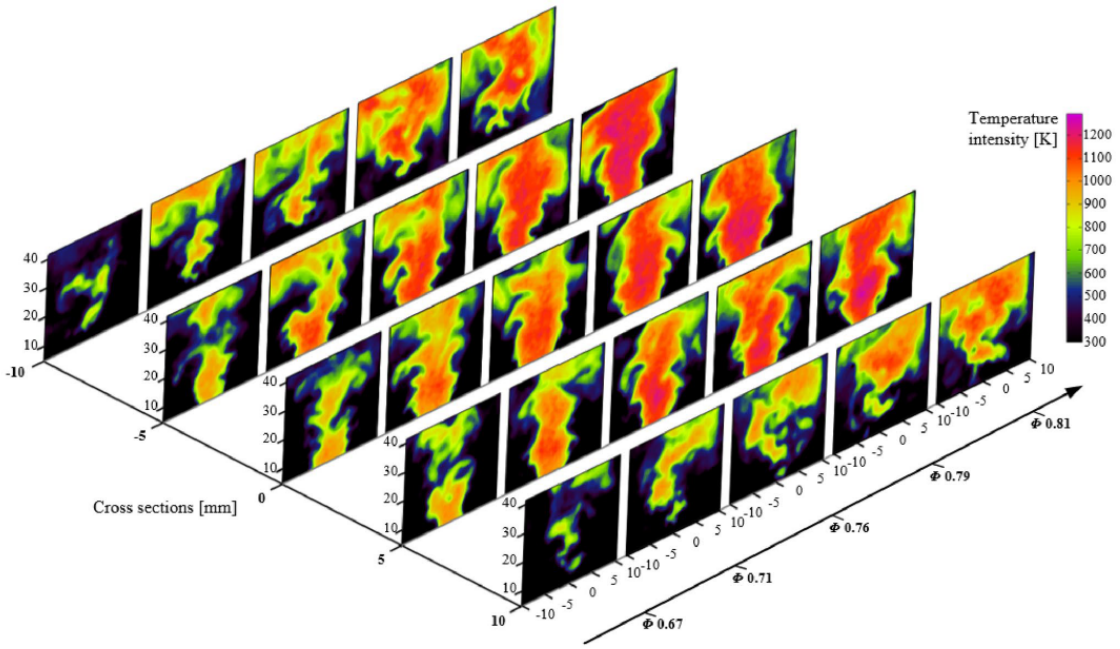

Figure 7: Instantaneous FRS temperature measurements made in a confined swirling methane/air flame from Li et al. [105].

Kearney et al. [106, 107] also calculated the differential scattering cross section using the nitrogen-only assumption and documented static temperature measurements in premixed methane/air flames that underestimated temperature by as much as 150 K when compared to adiabatic flame temperature calculations and CARS temperature measurements. This bias is similar to the levels of uncertainty documented by Elliot et al. [84, 100] using the same assumption. Kearney et al. found large improvements in measurement accuracy using the equilibrium flame mixture composition to calculate the differential scattering cross section.

As the flow complexity increases, higher fidelity modeling of the combustion process must be used to calculate the differential scattering cross section. For example, Krishna et al. [108] performed kHz-rate FRS thermometry in the narrow channels of a flame arrestor model to study flame quenching and divided the propagating flame into four separate regions. In some regions, the composition was calculated assuming an adiabatic product composition. In other regions, a model for gas composition as a function of temperature was derived by analytically simulating a strained laminar flame with heat loss. This modeling strategy allowed them to measure the temperature in the channel as the flame evolved in time, which revealed the temporal evolution of the flamefront. These results are shown in Figure 8.

In some complex flows, such as nonpremixed flames, even advanced modeling strategies cannot accurately predict the spatiotemporal variation in mixture

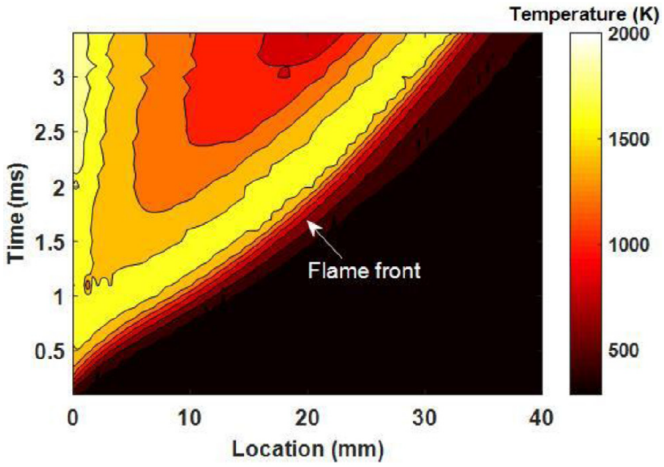

Figure 8: Temporal evolution of a premixed methane/air flame propagating in a narrow channel from Krishna et al. [108].

composition. In such cases, simultaneous measurement of mixture composition might be required for accurate FRS temperature measurements. For example, in a nonpremixed driven diffusion flame, Kearney et al. [107] used FRS temperature imaging combined with simultaneous Raman scattering measurements of the gas composition to correct for local variations in the differential scattering cross section. This was the first application of 2-D FRS thermometry in a nonpremixed flame. Müller et al. [92] also used Raman scattering to simultaneously measure local gas composition in conjunction with FRS static temperature measurements in a premixed particle-loaded propane/air flame.

In the absence of simultaneous Raman scattering mixture composition measurements, which are not feasible in many cases, one way to enable FRS temperature measurements in nonpremixed flames is through a concept known as fuel tailoring. This process, documented for FRS by McManus and Sutton [61, 109], entails the careful selection of a specific fuel mixture that minimizes the variation of the mixture-averaged properties across the flame. Fuel-tailoring has a history of use in unfiltered Rayleigh scattering thermometry, with the best example being the DLR standard flame whose specific mixture of methane/hydrogen/nitrogen was tailored so that its Rayleigh scattering cross section was similar to that of air and varies only ±3% across the mixture fraction space [110].

McManus and Sutton extended the fuel-tailoring concept to FRS. The procedure of selecting fuel composition is less straightforward for FRS because the measured signal depends on both the local mixture-averaged cross section and the numerous species-dependent Rayleigh lineshapes. Using a series of opposed-flow, nonpremixed, laminar flame calculations, McManus and Sutton designed a fuel that is composed of 16% methane, 16% hydrogen, and 68% argon. Its mixture-averaged differential scattering cross section varies by only 1.5% across the mixture fraction space and the "figure of

merit", $\mathcal{F}$, is approximately equal to one:

$$\mathcal{F} = \sum_n \left[\chi_n \frac{\mathrm{d}\sigma}{\mathrm{d}\Omega_n} \int_{-\infty}^{+\infty} t\mathcal{R}_n \mathrm{d}\nu \right] \Bigg/ \left[\frac{\mathrm{d}\sigma}{\mathrm{d}\Omega} \int_{-\infty}^{+\infty} t\mathcal{R} \mathrm{d}\nu \right]_{\mathrm{air}} \approx 1. \tag{11}$$

This tailored fuel mixture allows them to use the scattering cross section and lineshape of air in the temperature calculation instead of those of the individual flame species. They verified the mixture's suitability for both FRS and unfiltered Rayleigh scattering thermometry (LRS) by performing measurements with both techniques simultaneously. The results of these measurements, along with the analytical variation of the figure of merit and temperature across the mixture fraction space are reproduced in Figure 9.

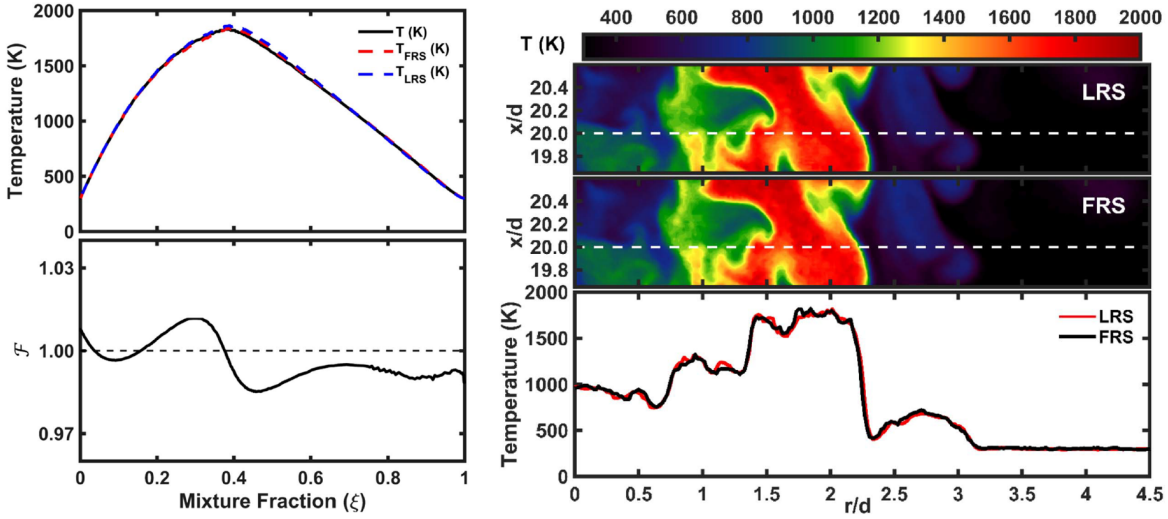

Figure 9: (Top left) Comparison between simulated flame temperature and the expected FRS and LRS thermometry measurements across the mixture fraction space. (Bottom left) Variation in the figure of merit across mixture fraction space. (Top right) Instantaneous flame temperature measurements from LRS and FRS. (Bottom right) Extracted LRS and FRS temperature measurements at x/d = 20, all from McManus and Sutton [61].

3.1.2. Measurements in Seeded Flames. FRS can also be used to nonintrusively measure static temperature in particle-laden environments. These environments either have naturally occurring particulates, such as soot, or tracer particles purposefully seeded into the flow. Seeded environments enable a unique capability to simultaneously measure temperature fields with FRS and 2-D velocity fields with PIV. The first demonstrations of simultaneous FRS and PIV measurements were documented in 2001 by both Elliot et al. [84] and Most and Leipertz [102]. Both groups performed their measurements in a premixed methane/air flame and noted several challenges: (1) the scattering of light from PIV particles can overwhelm the FRS signal if the particle density is too high, which limits the spatial resolution of the velocity measurements, and

(2) regions around larger particle agglomerates that are not sufficiently filtered have to be removed in post-processing and interpolated in the FRS temperature field. Despite the above challenges, both groups were able to obtain simultaneous measurements of temperature and velocity in a turbulent flame, which provided insight into the local interaction of combustion and turbulence.

McManus and Sutton [101] developed a novel approach for eliminating the cross-talk between the PIV and FRS measurements. Instead of using a frequency-doubled Nd:YAG for both the PIV and FRS, they applied these techniques at two different frequencies. The FRS measurements were performed with the typical frequency-doubled Nd:YAG/iodine absorption cell laser/filter combination, but the PIV measurements were performed with a double-pulsed 532 nm PIV laser pumping a dye laser that emitted at 568 nm. The 532 nm FRS pulse was emitted in between the two laser pulses of the PIV system. This spectral and temporal separation allowed for much higher spatial resolution of the PIV and FRS measurements. The authors report that the FRS resolution was sufficient to resolve the Batchelor scale, the smallest length scale before the dissipation of a scalar fluctuation. Sample simultaneous temperature and velocity fluctuations obtained from these measurements are shown in Figure 10. Having high-resolution simultaneous temperature and velocity fluctuation data are crucial for turbulence model development where the turbulent temperature flux and species mass fraction fluxes are important unclosed terms in need of high-quality data for model verification and validation.

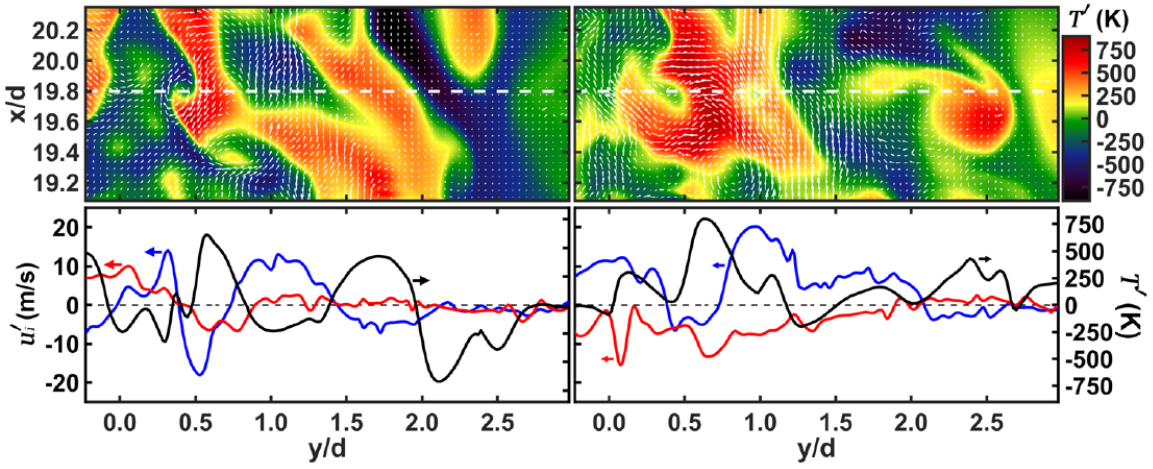

Figure 10: (Top) Sample simultaneous temperature and velocity fluctuation fields from McManus and Sutton [101]. (Bottom) Fluctuations of temperature (black), axial (blue), and transverse (red) velocity fluctuations extracted from the x/d = 19.8 axial station.

3.2. Mixture composition

A powerful feature of FRS is its ability to quantify the composition of binary gas mixtures. These experiments are typically designed to study the fundamental physics of

the mixing process of two dissimilar gases, such as a nonreacting fuel (or fuel simulant) and air. While air is itself a mixture, it can be treated as a single species with mixture-averaged thermophysical and transport properties [111]. Mixture composition can be measured because each species has a unique differential scattering cross section, $\frac{\mathrm{d}\sigma}{\mathrm{d}\Omega}$, and lineshape, $\mathcal{R}$. The FRS signal variation caused by a change in gas composition is often assumed to be due solely to the differential scattering cross section term because it has a stronger dependence on the gas composition than the integrated lineshape [45, 93]. Consequently, experiments are typically designed to isolate the signal's dependence on the differential scattering cross section.

One way to measure the time-average composition of a binary mixture of air and another species with FRS is to use a ratiometric approach. This technique was first used in unfiltered Rayleigh scattering experiments in the early 1980s and traces its roots back to the work of Dyer [14] and Pitts and Kashiwagi [112]. The ratiometric approach can be similarly implemented with PLIF, although with the additional complexities introduced by the fluorescence and quenching processes [113, 114]. This technique relies upon taking measurements of a mixing experiment operating at two different conditions with the same optical setup. The first operating condition is the mixing flowfield of interest, where the target species is injected into the relevant air environment. In the second operating condition, the air environment remains the same and the target species is replaced with an air stream that is injected in its stead. The injected air stream should, ideally, have the same number density as the fuel stream. To calculate the time-average mole fraction of the target species, the following equation is used:

$$\overline{\chi}_f = \frac{\bar{S}_{ao} - \bar{S}_f}{\bar{S}_{ao}} \left(\frac{1}{1 - \frac{(d\sigma/d\Omega)_f}{(d\sigma/d\Omega)_a}} \right), \tag{12}$$

where the subscript f indicates the signal when the target species is injected (condition 1), the subscript ao indicates the signal when only air is present (condition 2), and $\frac{(d\sigma/d\Omega)_f}{(d\sigma/d\Omega)_a}$ is the ratio of the differential scattering cross sections for the target and air species. In order to achieve the maximum sensitivity in the mixture composition measurement, the difference in the scattering cross sections between the two streams should be as large as possible. Helium is a popular choice for the fuel stream because it has a scattering cross section approximately 73 times smaller than that of air and can be said to mimic the dynamic behavior of hydrogen due to their similar molecular weights. Heavier hydrocarbon fuels can also be used because they have scattering cross sections that are as much as 10-15 times larger than that of air. A more detailed derivation of Eq. 12 can be found in Gopal and Maddalena [45, 115] who also discuss the assumptions required to use the equation and the resulting uncertainties of the method.

The ratiometric method was first used in an FRS experiment by Seasholtz and Buggele [19]. They studied the transverse injection of a sonic jet of helium into a Mach 3 crossflow and quantified the jet penetration and helium mole fraction in the mixing region. These mole fraction measurements had large uncertainties (with a standard

deviation of χ_{He} approx $0.1 - 0.2$) due to incomplete filtering of the stray background light, which resulted in signal-to-noise ratios smaller than desired. Nevertheless, they were able to demonstrate the feasibility of the technique. This approach was also used by Maddalena et al. to quantify the time-averaged mixture composition of supersonic flowfields dominated by streamwise vortices at conditions relevant to scramjet-powered hypersonic flight [45, 94, 115, 116, 117]. In these experiments, helium was injected through a ramped-strut injector to simulate the dynamics of hydrogen fuel. The FRS helium mole fraction measurements were compared with an aspirating gas-sampling probe whose measurements were in good agreement with the FRS results [118, 119]. Average FRS helium mole fraction contours from these experiments are reproduced in Figure 11.

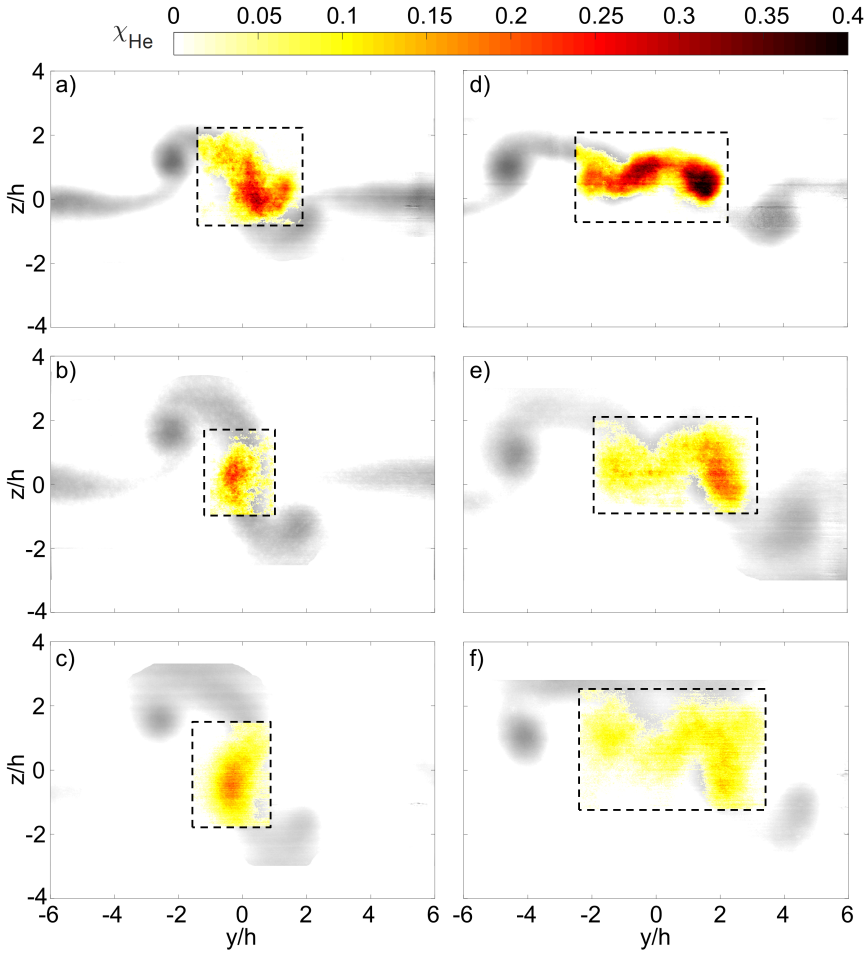

Figure 11: Average FRS helium mole fraction contours from Ground et al. [94]. (a)–(c): merging vortex interactions at distances 10, 16, and 20 ramp heights downstream of the injection plane. (d)–(f): nonmerging vortex interaction. The grey-scale fuel plume outline is depicted behind the helium mole fraction contours in the dashed box. The y and z coordinates are normalized by, h, the vortex-generating ramp's height.

While the ratiometric technique can only be used to obtain time-average measurements of binary mixture composition, FRS can also be used to obtain mixture

composition measurements from a single image. This is generally accomplished when the variation in a calibrated and normalized FRS signal is a function only of the local mixture composition. Reeder et al. [73, 74] designed such an experiment and used FRS to quantify the core jet trajectory and mixing rate of buoyant helium and carbon dioxide jets issuing into air using a CW laser. They identified jet features that influence the gross mixing rate, such as side jets that expel fluid from the core. These can be seen in Figure 12. Benhassen et al. [120, 121] also studied buoyant CO_2 jets and characterized the resulting flowfields with a similar continuous wave laser setup at a sampling rate of 400 Hz.

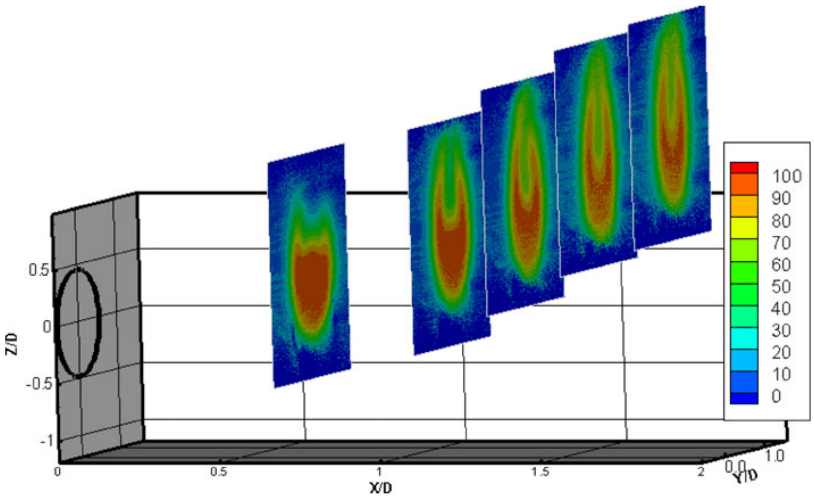

Figure 12: FRS measured helium mole fraction contours of a buoyant jet from Reeder et al. [74].

Krishna et al. [96] used a 1-D FRS instrument to measure the mole fractions of nonreacting methane and air in a transparent conical quarl burner. Here, the 1-D instrument allowed for higher measurement precision with a 95% confidence interval of 0.02 in the mean methane mole fraction. This 1-D technique has many advantages over 2-D FRS imaging. For instance, a 2-D laser sheet inherently has lower energy density and suffers from shot-to-shot spatial variation in the laser sheet profile. Given the highly accurate 1-D measurements collected by Krishna et al., this work has the ability to support numerical validation of swirling quarl flows.

Finally, a novel implementation of FRS mixture composition measurement was demonstrated by Allison et al. [93] who measured the mole fraction of an evaporating hydrocarbon fuel spray flow. The FRS technique allowed for gas-phase composition measurements to be made in the presence of liquid-phase droplets by filtering out the Mie-scattered light from the liquid fuel droplets. Simultaneous Mie-scattering images were used to visualize the liquid-phase. Results from this experiment are shown in Figure 13.

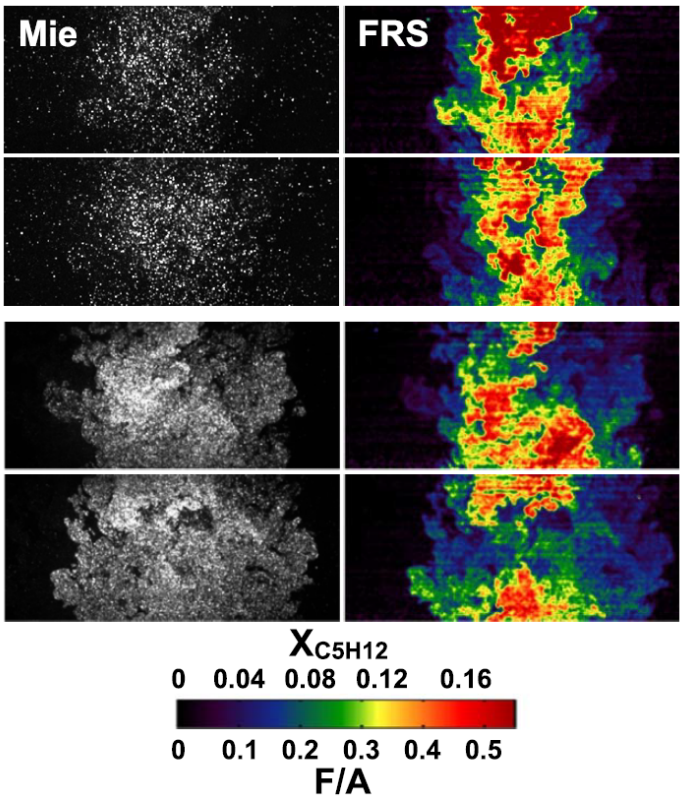

Figure 13: Mie scattering and FRS gas-phase composition measurements from an evaporating fuel spray flow [93].

3.3. Other Single Property Measurements

Similar to the ratio method for static temperature measurements, a few research groups have acquired single property density or pressure measurements under conditions where the sensitivity of the FRS signal to temperature and velocity is purposefully attenuated. For example, George et al. [122] made measurements of density in an underexpanded Mach 1.4 jet. The FRS signal was made primarily a function of the flow density by (1) placing the detector at a viewing angle that eliminates the sensitivity of the FRS signal to the bulk velocity of the jet and (2) tuning the central frequency of the illuminating laser to the edge of an absorption feature. By ratioing the recorded signal to a signal at a known reference condition, quantitative density measurements were made. These measurements agreed acceptably with unfiltered Rayleigh scattering density measurements of the same flow.

In a similar vein, Hunt et al. [59, 123] showed that by optimizing both the central frequency of the illuminating laser and the direction of the observation vector, it is theoretically possible to obtain density measurements in an oblique shock train with a median error as low as 0.58%. Feng et al. [124, 125] also studied the sensitivities of the model FRS signal equation. By carefully selecting the central frequency of the illuminating laser, the direction of the observation vector, and the iodine filter vapor

pressure, they created an optimized experimental setup that reduced the sensitivity of the FRS signal intensity ratio to temperature. The insensitivity to temperature allowed for the pressure across a blast wave to be measured with a 7% uncertainty. The drawback of these techniques is that they require the ability to arbitrarily position the detector to optimize the direction of the observation vector, which is not possible in confined flows with limited optical access.

The last relevant fluid dynamic property that has not been discussed within the framework of single property FRS measurements is velocity. Such measurements can be made from scattering from nanoscale solid or liquid particles, such as a condensed vapor or fog. Rayleigh scattering from particles differs from pure molecular scattering in that the scattering profile is not thermally broadened and is assumed to have a linewidth equal to that of the illuminating laser. The lack of thermal broadening removes the dependence of the scattered light's spectral profile on the thermodynamic properties of the gas in which the particles exist. Thus, the spectral profile of the scattered light is simply Doppler shifted compared to the incident light. When a molecular absorption filter is used in conjunction with a signal and reference detector, instantaneous measurements of gas velocity can be made. While some authors have called this measurement "FRS velocimetry" [41], it is more commonly known as Doppler global velocimetry (DGV) or planar Doppler velocimetry (PDV). The development of DGV was first described in the literature by Komine et al. [72] around the same time that Miles et al. [26, 30] first detailed FRS. Since PDV/DGV is at its crux a particle-based technique that often requires flow seeding, we consider it to be a separate technique entirely from FRS despite the similarities. Reviews of PDV/DGV can be found elsewhere in the literature [126, 127, 128].

Alternatively, flow velocity can be measured with FRS without taking advantage of a naturally occurring condensation process or flow seeding. However, the techniques that enable measurement of velocity from molecularly scattered light typically also allow for other flow properties to be measured simultaneously. These techniques are discussed in the following section.

3.4. Multiple property measurements

One of the most powerful features of FRS is its ability to measure multiple flow properties simultaneously. There are several ways to approach simultaneous property measurement with FRS and each method is briefly reviewed here.

3.4.1. Time-averaged multiple property measurements. The first multiproperty FRS measurement technique was proposed by Miles et al. [26, 30, 60]. This method involves scanning the incident laser central frequency, ν_c, over an absorption feature while the filter transmission profile remains constant, as illustrated in Figure 14(a)–(e). The FRS signal, S, at each step depends on the position of ν_c with respect to the transmission profile, t. Figure 14(f) shows the plot of S versus ν_c, which provides spectral information

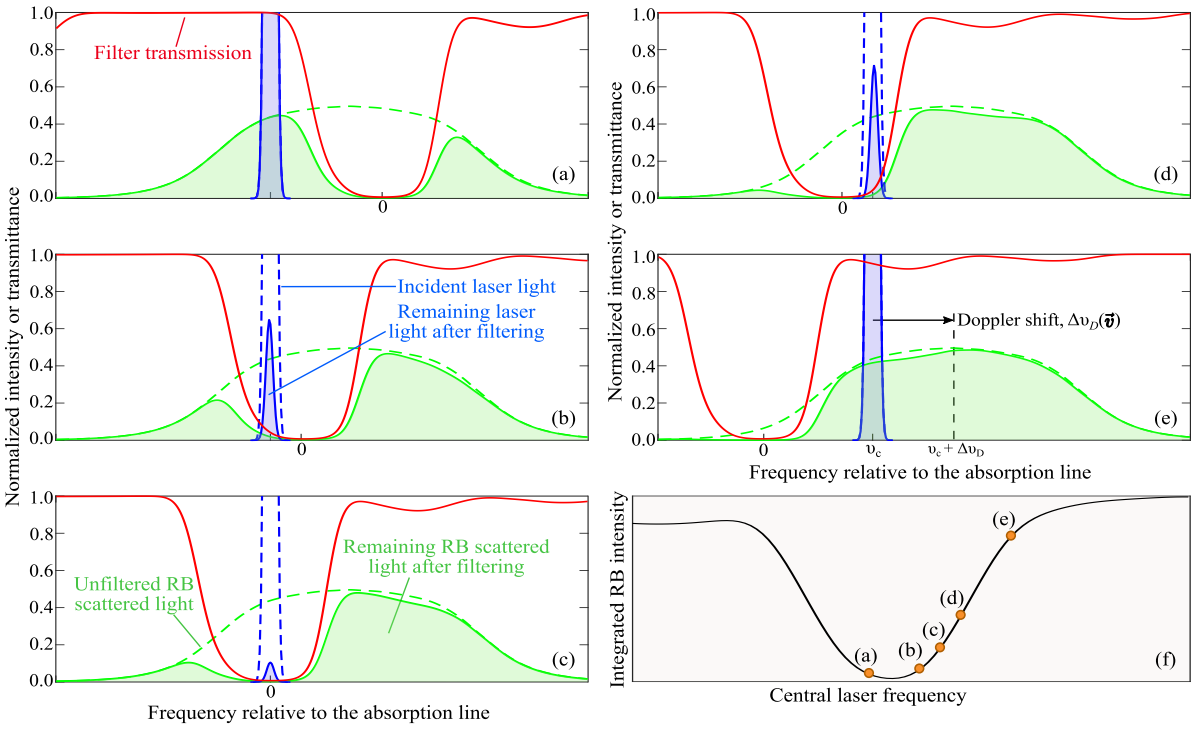

Figure 14: Representation of FRS scanning technique.

about the Rayleigh scattered light that is lost in typical integrated FRS intensity measurements. Since S is related to the convolution of the Rayleigh scattered lineshape, $\mathcal{R}$, with the filter transmission profile, t, the curve of S versus ν_c is sometimes called the FRS convolution spectrum.

If the composition of the gas is known, the shape and relative position of the convolution spectrum are a function of the flow velocity, pressure, temperature, and density. Specifically, the shift in the minimum of the convolution spectrum relative to the minimum of the filter's transmission profile is used to determine the flow velocity in the $(\hat{\mathcal{O}}-\hat{\mathcal{L}})$ direction (see Equation 5). The magnitude and shape of the spectrum, along with an equation of state, can then be used to recover the flow pressure, temperature, and density.

Because the frequency scan takes time to complete, the flow properties recovered from the convolution spectrum represent an average of the flow properties over the period of the scan. Typically, multiple intensity measurements are acquired at each discrete frequency in the scan and are averaged to reduce measurement noise. For 2-D measurements, a series of images would be recorded with each resolution element in the image having its own convolution spectrum. In this way, multiple flow properties across an entire 2-D image plane can be determined. The sharp cutoff features and narrow widths of the molecular notch filters employed in FRS mean that frequency scans have a bandwidth of a few GHz (typically, ≤ 5 GHz).

Flow properties are recovered from the FRS convolution spectrum by fitting the experimentally measured spectrum with analytically generated model spectra. Using

classical least-squares-based minimization methods (e.g., Levenberg-Marquardt), the Doppler shift, pressure, and temperature that minimize the difference between the experimental spectrum and the model spectra are found. When calculating the model convolution spectra, the flow properties must be the only unknowns. Therefore, the optical properties of the system must be completely known, including the catch-all optical efficiency parameter A in Equation 1. This parameter is often determined through a calibration experiment at a reference condition where the only unknown is the efficiency parameter A. As discussed by Doll et al. [50], some experimental arrangements are not conducive to an in situ calibration. In such cases, it is possible to normalize the model equation such that A does not need to be known; however, this comes at a steep penalty as the normalized model equation's sensitivity to pressure is decreased by more than an order of magnitude.

Ideally, the fitting process uses a full-bandwidth scan, such as the one depicted in Figure 14(f). However, this is only possible when there is little to no interference from background scattered light. In such cases, the filter is not necessary for background light removal and is instead used to resolve spectral features of the Rayleigh scattered light through the convolution procedure. If the filter is needed to remove background scattering, the bandwidth of the scan must be limited to frequencies where the background is sufficiently attenuated (e.g., the range represented by Figure 14b-d) [67].

Though limiting the scan makes the fitting process more challenging, Boyda et al. [42] have proven that it is still possible to obtain multiple flow properties from truncated convolution spectra. The same authors also point out that one way to improve the accuracy of velocity measurements from truncated convolution spectra is to use a cross-correlation method to determine the Doppler frequency shift before using least-squares fitting to determine the remaining flow properties. This method traces its roots to the cross-correlation Doppler global velocimetry technique developed by Cadel and Lowe [129].

The frequency scanning method was further refined by Forkey et al. [62, 87, 130] who documented the full capability of the technique in a series of works. This work culminated in the simultaneous measurement of the average flow temperature, pressure, and a single velocity component across a 2-D plane in a Mach 2 free jet [39]. An error analysis of these measurements estimated that the uncertainties in the velocity, temperature and pressure measurements were $\pm 2-3\%$, $\pm 2\%$, and $\pm 4-5\%$, respectively, with the majority of the uncertainty stemming from the 1° uncertainty in the angle between the laser propagation vector and the observation vector.

Boguszko and Elliot [84, 131, 132, 133] later used the frequency scanning method to characterize two distinct types of fluid flows: a free jet and the flowfield created by laser-induced energy deposition in quiescent air. For the free jet experiment, they performed high-resolution 120-point scans through the iodine absorption line centered near $18,789.28$ cm^{-1} and acquired 50 instantaneous images at each of the 120 discrete frequencies. Despite having four times as many points in the frequency scan, Boguszko and Elliot found similar amounts of uncertainty in their free jet property measurements

when compared to the work of Forkey, with uncertainties of ±1.6% in temperature, ±5.9% in pressure, and ±2.9% in velocity. The uncertainty of the viewing angle and the central laser frequency were the most dominant uncertainty sources. In the laser-induced energy deposition experiment, Boguszko and Elliot quantified the flowfield properties around the shockwave generated by the optically-induced air breakdown at various times after the initial energy discharge. For each time delay, measurements were made by tuning the laser to an initial frequency, acquiring a set of 200 reference images without the energy deposition, then acquiring a set of 200 images with the deposition that were later ensemble averaged. The laser was tuned to a new frequency and the process was repeated until the entire absorption feature was scanned through. These pressure, temperature, and velocity measurements agreed with a computational model of laser energy deposition within the estimated uncertainty bounds of the technique. Examples of these pressure measurements are shown in Figure 15.

More recently, a group from the German Aerospace Center (DLR) implemented frequency scanning FRS in a wide variety of experiments. They have characterized flow planes inside of a bell-mouthed circular duct [67], a Ranque-Hilsch vortex tube [68], and downstream of a nozzle guide vane (NGV) cascade in a three-sector combustor simulator [95]. The DLR group has also characterized flow planes at the exit of a lean-burn single sector combustor [134, 135] and a subsonic turbulent jet [50, 69]. A unique feature of the DLR technique is that the scattered light signal is transferred through a fiber endoscope before it is routed to the front face of the iodine absorption filter ahead of the detector. Imaging with a fiber endoscope introduces additional complexities to the measurement (such as reduced spatial resolution and additional background light scatter occurring within the fiber bundle), but allows for measurements of internal flows and other flows not conducive to expansive optical access [67]. The DLR group has also used a set of three imaging fiber bundles, with each bundle viewing the Rayleigh scattered light from a different perspective, to make simultaneous planar pressure, temperature, and three-component velocity measurements of a turbulent jet [69]. These measurements agreed well with previously reported experimental measurements of self-similar jets, highlighting the ability of the frequency scanning FRS technique to completely quantify

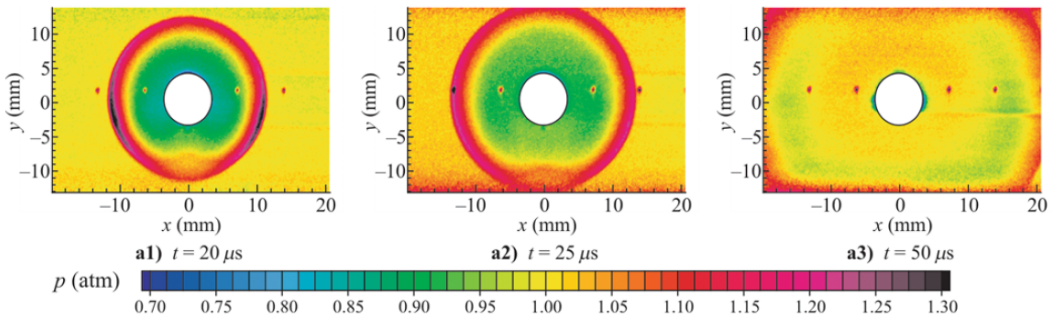

Figure 15: Pressure field around shockwave generated from laser energy deposition experiment at three different times post discharge. From Boguszko and Elliot [133].

the average properties of a flowfield when using multiple observation directions

In another impressive application of the frequency scanning FRS technique by the DLR group, Doll et al. [95] characterized the flow downstream of a NGV cascade, which had previously only been characterized via intrusive means. These FRS measurements were compared to five-hole probe measurements, which indicated that the pressure sensitivity of the FRS measurements was not good enough to resolve any probe-related interferences in the pressure field. However, the other measured quantities were in good agreement, as can be seen in Figure 16. The FRS measurements were also able to identify a bias in the axial velocity measurements of the five-hole probe that was confirmed via CFD. Overall, the group concluded that the frequency scanning FRS technique is a viable alternative to invasive probe-based techniques commonly applied in turbomachinery environments.

Apart from the DLR group, recent work utilizing frequency scanning FRS for multiple flow property measurement has been performed in a heated supersonic jet with a thermal nonuniformity by Saltzman et al. [70]. This setup had three independent imaging modules, which allowed for all three velocity components to be measured

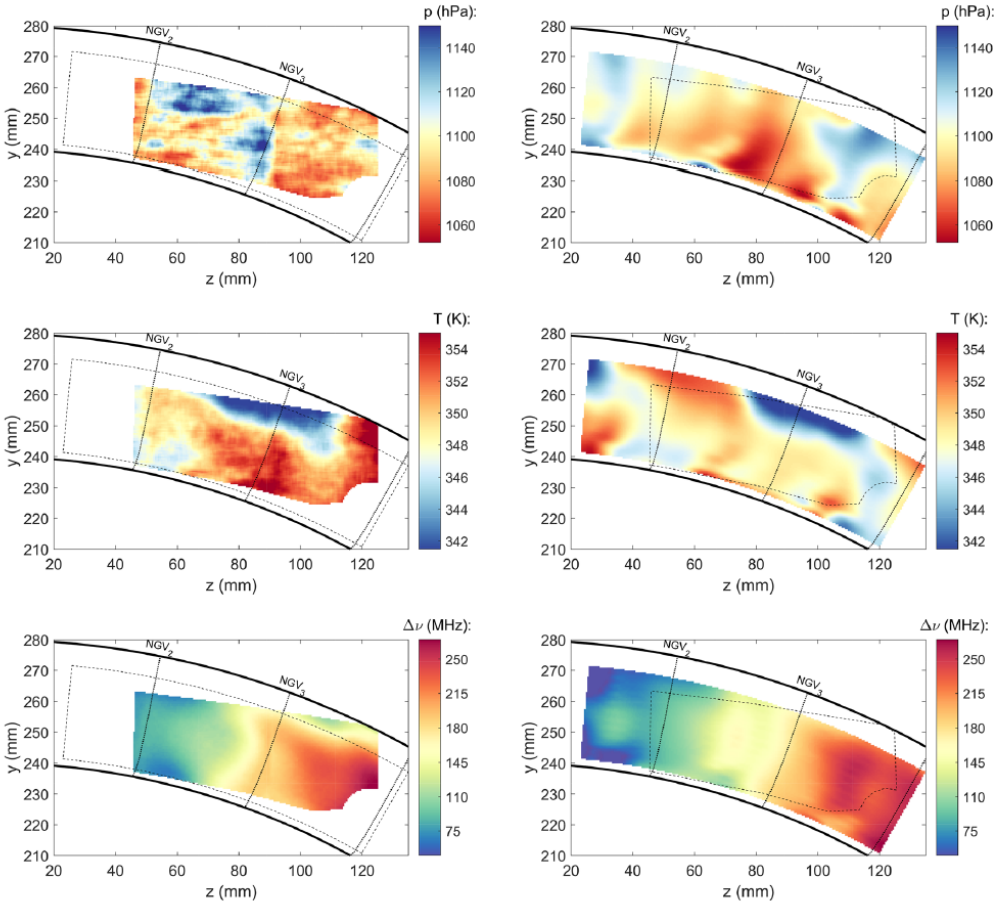

Figure 16: Pressure, temperature, and Doppler shift measured with frequency-scanning FRS (left column) and a five-hole probe (right column) behind a NGV cascade from Doll et al. [95].

in addition to static temperature. The jet velocity measurements were made at two downstream axial stations, both of which compared favorably to PIV velocity measurements, with a maximum discrepancy of 17 m/s at the supersonic jet centerline. The work of Saltzman et al. utilized the data analysis methods documented by Boyda et al. [42, 43] to account for interference from Mie scattered light and to document the uncertainty of the measurements.

3.4.2. Instantaneous multiple property measurements. The frequency scanning FRS technique is a versatile and reliable measurement tool for a wide variety of flows, but this method has a significant shortcoming: it is only able to measure time-averaged flow properties over the amount of time it takes to perform a laser wavelength scan. Researchers have long desired to perform instantaneous, spatially-resolved, multiproperty measurement with FRS. Though several techniques of this type have been proposed, thus far none have achieved the fidelity of the frequency scanning method for average property measurement. However, recent work shows that significant strides are being made within this research area.

The quantification of multiple instantaneous flow properties with FRS is a challenging task that requires obtaining several simultaneous and independent measurements of the flow under investigation. If the number of independent FRS measurements is equal to the number of unknown flow properties, then a system of FRS signal equations (i.e., Equation 3) can be compiled and solved uniquely. Miles and Lempert [30] proposed the first instantaneous, two-dimensional, multiproperty FRS measurement technique. Though they did not perform the experiment, Miles and Lempert detailed how a single view of an FRS experiment could be routed to four different detectors using a series of beam-splitting optics with three of the detectors placed behind absorption filters. If each of the three filters have unique transmission profiles (which can be achieved by altering the thermodynamic properties of the absorbing gas, see Section 2.3.2), then this setup yields a unique solution for any combination of density, velocity, and temperature.

The multiple filter method was trialed by George et al. [136] using photomultiplier detectors to make single-point measurements of temperature and velocity in a supersonic jet. These measurements followed expected trends, thus demonstrating the feasibility of the multiple filter technique. However, the sensitivity of their measurements was less than predicted which resulted in large measurement uncertainty. Jenkins et al. [137] built upon the FRS measurement sensitivity analysis of Feng et al. [125, 138] to show that increased measurement sensitivity relative to the results of George et al. [136] could be theoretically obtained in a multiple filter setup, but did not confirm the results with experimental measurements. Recently, Feng et al. [139] devised a two-filter setup for the simultaneous measurement of density and one velocity component in a supersonic jet that agreed well with Pitot probe calibration data, but their measurements have uncertainties ranging from 19% to 23%.

Boguszko [140] proposed a four-camera, three-filter arrangement for the

simultaneous determination of two velocity components, density, and temperature. However, the signal to noise ratio of the measurements was too low to achieve reliable results. Yeaton et al. [141] proposed a technique for spatiotemporally resolved measurements of temperature and density utilizing two iodine filters and two separate detectors each comprised of a compact two-dimensional array of solid state photomultipliers. The filters were carefully selected with different absorption properties such that one detector's FRS signal is primarily sensitive to temperature and the other's is primarily sensitive to density. Proof-of-concept measurements were made using one of the two filters and the simultaneous two filter technique was only analyzed analytically.

Building upon their experience with time-averaged multiproperty FRS measurements, Doll et al. [71] have proposed two concepts for instantaneous measurement of three-component velocity, temperature, and pressure, which are depicted schematically in Figure 17. Both concepts rely upon the use of imaging fiber bundles to provide multiple independent views of the measurement region. In one concept, there is a single filter and detector, meaning that at least five independent views are required to close the system of equations and uniquely determine the flow properties. In the second concept, a second detector and a filter with a different transmission profile are added to the setup. This reduces the number of independent views required to three. Doll et al. used a multiobjective optimization procedure to determine the optimum observation directions for each concept in a subsonic ducted flow [142]. This optimization study concluded that the single filter and detector concept is superior because the addition of a second filter does not significantly improve flow parameter sensitivity even if the number of independent observation directions is the same for both concepts. Recently, Doll et al. [143] performed a proof-of-concept experiment in a simplified duct flow that demonstrated the data analysis procedure required to make time-resolved simultaneous property measurements by performing multiparameter analysis on a set of images obtained at a single discrete frequency in a frequency-scanning experiment. These results are shown in Figure 18. Although the quasi time-resolved measurements show increased spatial variance with respect to the time-averaged results ($\sim 10\%$ versus $\sim 1\%$), the spatial average of the quasi time-resolved measurements agree well with the frequency the frequency scanning results, albeit with much higher measurement uncertainty. Nevertheless, this promising result highlights the potential of the technique and the group expresses future plans to further develop the technique.

3.5. Quantification of Parameter Uncertainty

Thus far, measurement uncertainties have been reported for specific experiments and experimental approaches. Since explicit discussion of uncertainty calculations is often omitted in FRS literature, this section briefly provides an overview of the general approaches to uncertainty quantification (UQ) that are most often used for FRS experiments.

A popular UQ approach in FRS literature is the error propagation formula which

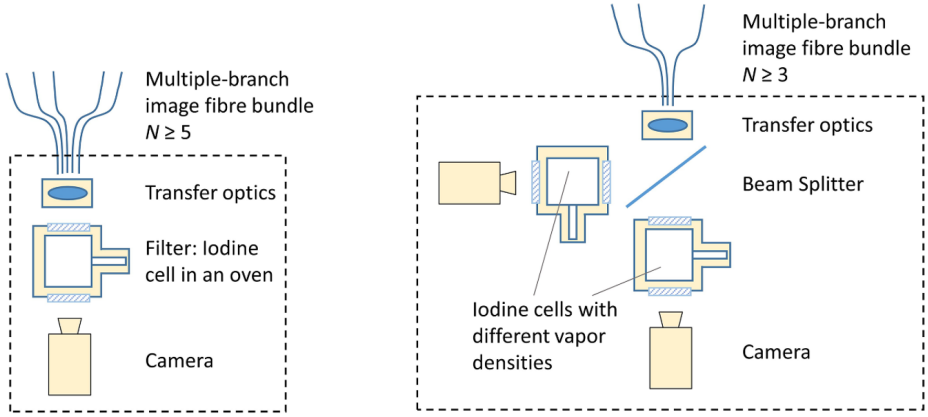

Figure 17: Concepts for instantaneous multiproperty measurement from Doll et al. [71].

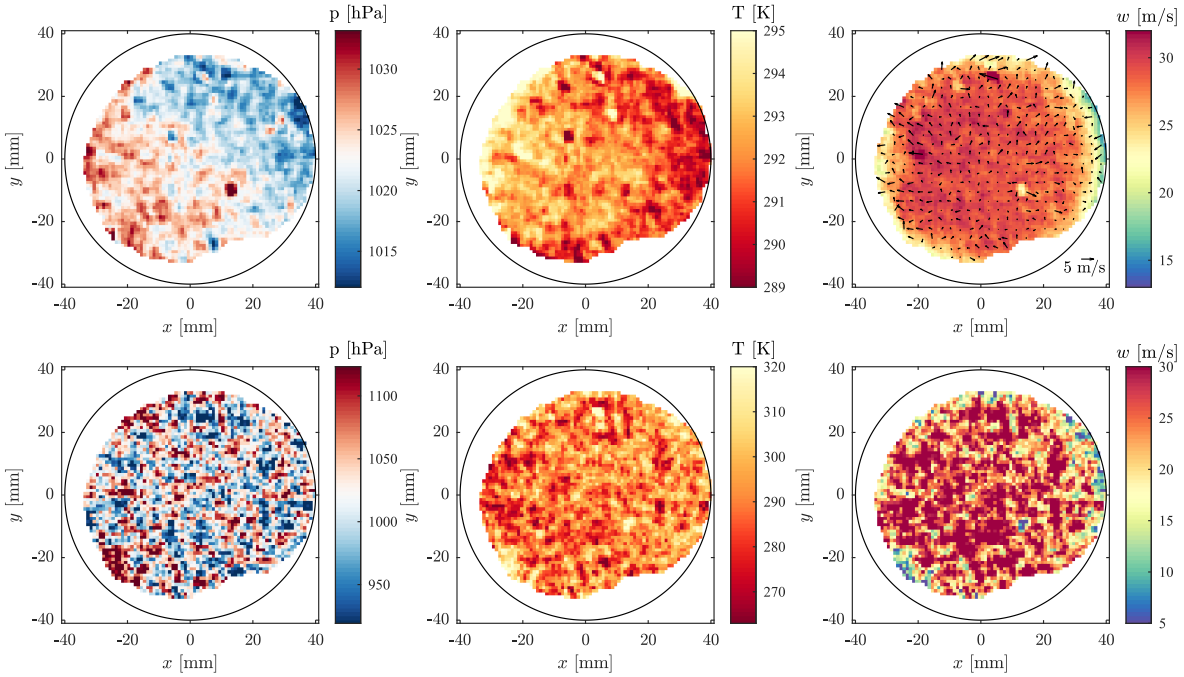

Figure 18: Frequency scanning FRS results (top) compared to quasi time-resolve FRS results (bottom) from Doll et al. [143].

approximates the uncertainty Δu of a quantity of interest (QOI) u as

$$\Delta u \approx \sqrt{\sum_i \left(\Delta u_i \frac{\partial u}{\partial u_i} \right)^2} \tag{13}$$

where Δu_i are the uncertainties of other parameters u_i[144]. As an example, consider estimating velocity in a 2-D flowfield by minimizing the difference between measured and theoretical pixel intensity (similar to Forkey et al. [145]). The velocity estimate is a function of experimental parameters like scattering angle θ or optical/experimental calibration parameters for the Rayleigh (R) and background (B) scattering. Given

known uncertainties in experimental parameters, e.g. $\Delta\theta$, ΔR, ΔB, Equation 13 yields $\Delta v \approx \sqrt{\Delta\theta^2 \frac{\partial v}{\partial \theta}^2 + \Delta R^2 \frac{\partial v}{\partial R}^2 + \Delta B^2 \frac{\partial v}{\partial B}^2}$. The derivatives may be calculated numerically by jittering the experimental parameters and observing changes to the estimate v. Among others, examples in the literature include Forkey et al., who use this approach to estimate uncertainty in velocity due to six experimental parameters, and Boguszko et al. where frequency scanning is used to measure temperature, pressure, and velocity in both a free jet and laser-induced energy deposition experiment [39, 41, 85, 100]

Equation 13 is derived from modeling uncertainties as standard deviations, the u_i as uncorrelated, and approximating the relationship between the QOI and other parameters with a first-order Taylor series [146]. Consequently, it works well when such assumptions are met, but less well under violations like very non-Normal uncertainty distributions, correlated u_i, or highly nonlinear or non-differentiable relationships. A nice property of this formula is that the constituents $(\Delta u_i \frac{\partial u}{\partial u_i})^2$ may be interpreted as the contribution of u_i to the variance of u.

The other major approach to uncertainty quantification is Monte Carlo (MC) simulations. For example, Doll et. al. use MC simulations to assess uncertainty in a frequency scanning FRS experiment recovering flow pressure, temperature and velocity [50]. Given assumed uncertainty distributions of the u_i, the MC approach generates many random samples of the u_i and propagates them to obtain a subsequent collection of random realizations of u. Uncertainty is then summarized, for example, as the standard deviation of the realizations of u. Applying this approach to the previous example, one might (1) assume θ, R, and B are independently Normal with standard deviations $\Delta\theta, \Delta R, \Delta B$, (2) generate many random realizations following these distributions, (3) use each random set of parameters to find v, and then (4) report the standard deviation of the different observed values of v.

As compared with the error propagation formula, the MC approach does not require that the u_i are uncorrelated nor does it use a Taylor approximation. Both approaches typically require calculating u under many choices of u_i as part of either numerically estimating a derivative or MC propagation. Both approaches also require some prior knowledge about the uncertainty of the experimental parameters (either their standard deviation or whole distribution).

4. Conclusion and Future Trends

This article began by reviewing the fundamental theory of filtered Rayleigh scattering and discussing spectral lineshape modeling. We then discussed considerations for selecting the three main components of an FRS system: the laser, molecular filter, and detector. An in-depth survey of the literature was provided, describing how the FRS signal equation can be manipulated to measure the thermodynamic gas properties of interest, before providing a brief discussion of uncertainty quantification as it relates to FRS measurements.

As this review has illustrated, filtered Rayleigh scattering has proven to be a

highly versatile tool that is capable of nonintrusively measuring various flow properties, including velocity (up to three components), temperature, pressure, density, and binary mixture composition in a wide variety of flows, ranging from sub- to supersonic speeds. FRS has several distinct advantages over many of the other laser-based diagnostic techniques used within the aerospace field, primarily owing to the fact that it is a molecular scattering technique that does not require the seeding of a particulate or fluorescent flow tracer. Also, due to the addition of the notch filter, which attenuates geometric scattering, FRS can achieve near-wall measurements that have long been challenging with other diagnostic techniques such as PIV. Another highly attractive feature of FRS is that it is accessible to a wide range of aerospace research groups because it can be executed with relatively accessible laboratory grade lasers and detectors. This fact has led to its increasing adoption and hastened development within the past several years.

Due to the increased attention being paid to the technique, the future prospects for FRS are very bright. FRS has already proven to be able to make highly accurate time-averaged measurements of multiple flow properties simultaneously with the frequency scanning technique. However, the true panacea of the nonintrusive gas diagnostic field is to be able to make instantaneous, time-resolved, measurements of multiple flow properties simultaneously across a 2-D flow plane. It is here where FRS has its most exciting prospects. The possibility of making such measurements with FRS was proposed in the very early FRS works [26] but, due to the laser and detector technology available at that time, researchers were not able to obtain a SNR high enough to successfully demonstrate the technique. While they still require further refinement in order to mature into more reliable methods, a few of the techniques presented in the very recent literature show true promise of achieving instantaneous multiproperty measurements. If the methods of increasing the spectral purity of current high-energy pulsed laser systems [65] can be combined with the instantaneous multiproperty measurement methodology of Doll et al. [71, 142, 143], the potential to reach the panacea of instantaneous multiproperty measurements could finally be realized. Another possible pathway to achieving these measurements is to use the demonstrated frequency-scanning capability of high-energy pulse-burst laser systems. Specifically, Fahringer et al. [147] have demonstrated that the frequency of a pulse-burst laser system can be scanned across an absorption feature multiple times during the 10.5 ms burst of laser pulses. They used this technique to acquire cross-correlation DGV measurements. If applied to frequency scanning FRS, this technique could greatly reduce the duration over which signals are averaged, thus allowing a more instantaneous type of measurement.

Other trends that are being explored include combining FRS with other diagnostic techniques, such as Raman scattering, Mie scattering, and PIV. These combined methods are a powerful way to reduce measurement error and gain additional simultaneous information about the flowfield. With laser equipment increasingly accessible and turn-key, these combined techniques that have been successfully, though

infrequently, demonstrated in literature are becoming more feasible. Furthermore, many laser diagnostic techniques, including FRS, are headed toward high frequency measurement rates with the increasing access to pulse-burst laser systems and high-framerate CMOS cameras. These time-resolved measurements are needed to study the dynamics that govern underlying flow problems, including turbulent flows, supersonic/hypersonic flows, and combustion. There are already several examples of such high-speed measurements acquired via unfiltered Rayleigh scattering [24, 98, 148, 149], interferometric Rayleigh scattering [32, 34], and PDV [150]. With regard to FRS, Lempert et al. [151] were early demonstrators of MHz FRS flow visualizations using an Nd:YAG pulse-burst laser. More recently, Krishna et al. [108] collected 10 kHz FRS thermometry measurements of a premixed flame in a narrow channel, also using a pulse-burst laser.

Overall, FRS has already proven itself to be a valuable diagnostic tool within the aerospace field. However, due the the advancements of laser and detector technology, the increased accessibility to commercial turn-key laser systems, and the increased methodological advancement of the technique by the many researchers deploying FRS in the field, FRS stands to see many exciting developments in the near future.

References

[1] Eckbreth A C 1996 *Laser Diagnostics for Temperature and Species in Unsteady Combustion* (Dordrecht: Springer Netherlands) pp 393–410 URL http://doi.org/10.1007/978-94-009-1620-3_18

[2] Danehy P M, Bathel B F, Johansen C T, Winter M, O'Byrne S and Cutler A D 2015 *Molecular-Based Optical Diagnostics for Hypersonic Nonequilibrium Flows* (AIAA) chap 8, pp 343–470 URL http://doi.org/10.2514/5.9781624103292.0343.0470

[3] Hassel E P and Linow S 2000 Laser diagnostics for studies of turbulent combustion *Measurement Science and Technology* **11** URL http://doi.org/10.1088/0957-0233/11/2/201

[4] Liu C and Xu L 2019 Laser absorption spectroscopy for combustion diagnosis in reactive flows: A review *Applied Spectroscopy Reviews* **54** 1–44 URL http://doi.org/10.1080/05704928.2018.1448854

[5] Steinberg A and Roy S 2023 *Optical Diagnostics for Reacting and Non-Reacting Flows: Theory and Practice* (American Institute of Aeronautics and Astronautics) URL http://doi.org/10.2514/4.106330

[6] Adrian R J and Westerweel J 2011 *Particle Image Velocimetry* 30 (Cambridge university press)

[7] Tropea C, Yarin A L and Foss J F 2007 *Springer handbook of experimental fluid mechanics* (Springer) URL http://doi.org/10.1007/978-3-540-30299-5

[8] Miles R B, Lempert W R and Forkey J N 2001 Laser Rayleigh scattering *Measurement Science and Technology* **12** R33–R51 URL http://doi.org/10.1088/0957-0233/12/5/201

[9] Goudin F C and Halthore R N 1986 Rayleigh scattering for density measurements in premixed flames *Experiments in Fluids* **4** 269–278 URL http://doi.org/10.1007/BF00369119

[10] Smith M, Smits A and Miles R 1989 Compressible boundary-layer density cross sections by UV Rayleigh scattering *Optics Letters* **14** 916–918 URL http://doi.org/10.1364/OL.14.000916

[11] Balla R J and Everhart J L 2012 Rayleigh scattering density measurements, cluster theory, and nucleation calculations at Mach-10 *AIAA Journal* **50** 698–707 URL http://doi.org/10.2514/1.J051334

[12] Panda J 2016 A molecular Rayleigh scattering setup to measure density fluc-

tuations in thermal boundary layers *Experiments in Fluids* **57** 1–10 URL http://doi.org/10.1007/s00348-016-2267-9

[13] Mercier B, Castelain T, Jondreau E and Bailly C 2018 Density fluctuations measurement by Rayleigh scattering using a single photomultiplier *AIAA Journal* **56** 1310–1316 URL http://doi.org/10.2514/1.J056507

[14] Dyer T M 1979 Rayleigh scattering measurements of time-resolved concentration in a turbulent propane jet *AIAA Journal* **17** 912–914 URL http://doi.org/10.2514/3.61247

[15] Escoda M C and Long M B 1983 Rayleigh scattering measurements of the gas concentration field in turbulent jets *AIAA Journal* **21** 81–84 URL http://doi.org/10.2514/3.8031

[16] Shirinzadeh B, Hillard M E, Balla R J, Waitz I A, Anders J B and Exton R J 1992 Planar Rayleigh scattering results in helium-air mixing experiments in a Mach-6 wind tunnel *Applied Optics* **31** 6529–6534 URL http://doi.org/10.1364/AO.31.006529

[17] Goix P J, Leonard K R, Talbot L and Chen J Y 1993 Direct measurement of mixture fraction in reacting flow using Rayleigh scattering *Experiments in Fluids* **15** 247–254 URL http://doi.org/10.1007/BF00223402

[18] Pitts W M 1996 Rayleigh light scattering for concentration measurements in turbulent flows NASA Conference Publication 10186, *Rayleigh Scattering Diagnostics Workshop*

[19] Seasholtz R G and Buggele A E 1997 Study of injection of helium into supersonic air flow using Rayleigh scattering *35th AIAA Aerospace Sciences Meeting and Exhibit* URL http://doi.org/10.2514/6.1997-155

[20] Brownell C J and Su L K 2011 Measurements of multiple mole fraction fields in a turbulent jet by simultaneous planar laser-induced fluorescence and planar Rayleigh scattering *Measurement Science and Technology* **22** 085402 URL http://doi.org/10.1088/0957-0233/22/8/085402

[21] Patton R A, Gabet K N, Jiang N, Lempert W R and Sutton J A 2012 Multi-kHz mixture fraction imaging in turbulent jets using planar Rayleigh scattering *Applied Physics B* **106** 457–471 URL http://doi.org/10.1007/s00340-011-4658-1

[22] Kampmann S, Leipertz A, Döbbeling K, Haumann J and Sattelmayer T 1993 Two-dimensional temperature measurements in a technical combustor with laser Rayleigh scattering *Applied Optics* **32** 6167–6172 URL http://doi.org/10.1364/AO.32.006167

[23] Böhm B, Frank J H and Dreizler A 2011 Temperature and mixing field measurements in stratified lean premixed turbulent flames *Proceedings of the Combustion Institute* **33** 1583–1590 URL http://doi.org/10.1016/j.proci.2010.06.139

[24] Grib S W, Jiang N, Hsu P S, Danehy P M and Roy S 2019 Rayleigh-scattering-based two-dimensional temperature measurement at 100-kHz frequency in a reacting flow *Optics Express* **27** 27902–27916 URL http://doi.org/10.1364/OE.27.027902

[25] Miles R B and Lempert W R 1997 Quantitative flow visualization in unseeded flows *Annual Reviews of Fluid Mechanics* **29** 285–326 URL http://doi.org/10.1146/annurev.fluid.29.1.285

[26] Miles R B, Lempert W R and Forkey J 1991 Instantaneous velocity fields and background suppression by filtered Rayleigh scattering *29th AIAA Aerospace Sciences Meeting and Exhibit* URL http://doi.org/10.2514/6.1991-357

[27] Grünefeld G, Beushausen V and Andresen P 1994 Planar air density measurements near model surfaces by ultraviolet rayleigh/raman scattering *AIAA Journal* **32** 1457–1463 URL http://doi.org/10.2514/3.12216

[28] Dam N J, Rodenburg M, Tolboom R A L, Stoffels G G M, Huisman-Kleinherenbrink P M and ter Meulen J J 1998 Imaging of an underexpanded nozzle flow by UV laser Rayleigh scattering *Experiments in Fluids* **24** 93–101 URL http://doi.org/10.1007/s003480050156

[29] Miles R and Lempert W 1990 Two-dimensional measurement of density, velocity, and temperature in turbulent high-speed air flows by UV Rayleigh scattering *Applied Physics B* **51** 1–7 URL http://doi.org/10.1007/BF00332317

[30] Miles R and Lempert W 1990 Flow diagnostics in unseeded air *28th AIAA Aerospace Sciences*

Meeting and Exhibit URL http://doi.org/10.2514/6.1990-62

[31] Bivolaru D, Ötügen M V, Tzes A and Papadopoulos G 1999 Image processing for interferometric Mie and Rayleigh scattering velocity measurements *AIAA Journal* **37** 688–694 URL http://doi.org/10.2514/2.796

[32] Mielke A F, Elam K A and Sung C 2009 Multiproperty measurements at high sampling rates using Rayleigh scattering *AIAA Journal* **47** 850–862 URL http://doi.org/10.2514/1.37369

[33] Sheng W, Jin-Hai S, Jun S, Zhi-yun H, Jing-feng Y and Jing-Ru L 2017 Two-dimensional interferometric Rayleigh scattering velocimetry using multibeam probe laser *Optical Engineering* **56** 111705 URL http://doi.org/10.1117/1.OE.56.11.111705

[34] Cutler A D, Rein K, Roy S, Danehy P M and Jiang N 2020 100-kHz interferometric Rayleigh scattering for multi-parameter flow measurements *Optics Express* **28** 3025–3040 URL http://doi.org/10.1364/OE.380934

[35] Cutler A D and Lowe K T 2023 *Laser Rayleigh scattering, filtered Rayleigh scattering, and interferometric Rayleigh scattering* (American Institute of Aeronautics and Astronautics) pp 75–136

[36] van de Hulst H C 1981 *Light scattering by small particles* (Courier Corporation)

[37] Bohren C F and Huffman D R 2008 *Absorption and scattering of light by small particles* (John Wiley & Sons) URL http://doi.org/10.1002/9783527618156

[38] McManus T A, Monje I T and Sutton J A 2019 Experimental assessment of the Tenti S6 model for combustion-relevant gases and filtered Rayleigh scattering applications *Applied Physics B* **152** URL http://doi.org/10.1007/s00340-018-7121-8

[39] Forkey J N, Lempert W R and Miles R B 1998 Accuracy limits for planar measurements of flow field velocity, temperature, and pressure using Filtered Rayleigh Scattering *Experiments in Fluids* **24** 151–162 URL http://doi.org/10.1007/s003480050162

[40] Patton R A and Sutton J A 2013 Seed laser power effects on the spectral purity of Q-switched Nd:YAG lasers and the implications for filtered Rayleigh scattering measurements *Applied Physics B* **11** 457–468 URL http://doi.org/10.1007/s00340-013-5358-9

[41] Boguszko M and Elliott G S 2005 Property measurement utilizing atomic/molecular filter-based diagnostics *Progress in Aerospace Sciences* **41** 93–142 URL http://doi.org/10.1016/j.paerosci.2005.03.001

[42] Boyda M T, Byun G and Lowe K T 2019 Investigation of velocity and temperature measurement sensitivities in cross-correlation filtered Rayleigh scattering *Measurement Science and Technology* **30** URL http://doi.org/10.1088/1361-6501/ab0350

[43] Boyda M T, Byun G, Saltzman A J and Lowe T 2020 Influence of Mie and geometric scattering contributions on temperature and density measurements in filtered Rayleigh scattering *AIAA Scitech 2020 Forum* URL http://doi.org/10.2514/6.2020-1516

[44] Tenti G, Boley C and Desai R 1974 On the kinetic model description of Rayleigh-Brillouin from molecular gases *Canadian Journal of Physics* **52** 285–290 URL http://doi.org/10.1139/p74-041

[45] Gopal V and Maddalena L 2021 Review of filtered Rayleigh scattering technique for mixing studies in supersonic air flow *Progress in Aerospace Sciences* **120** URL http://doi.org/10.1016/j.paerosci.2020.100679

[46] Vieitez M O, van Duijn E J, Ubachs W, Witschas B, Meijer A, de Wijn A S, Dam N J and van de Water W 2010 Coherent and spontaneous Rayleigh-Brillouin scattering in atomic molecular gases and gas mixtures *Physical Review A* **82** 043836 URL http://doi.org/10.1103/PhysRevA.82.043836

[47] Gu Z and Ubachs W 2014 A systematic study of Rayleigh-Brillouin scattering in air, N2, and O2 gases *The Journal of Chemical Physics* **141** 104320 URL http://doi.org/10.1063/1.4895130

[48] Gu Z, Ubachs W and van de Water W 2014 Rayleigh-Brillouin scattering of carbon dioxide *Optics Letters* **39** 3301–3304 URL http://doi.org/10.1364/OL.39.003301

[49] Letamendia L, Joubert P, Chabrat J P, Rouch J, Vaucamps C, Boley C D, Yip S and Chen S H 1982 Light-scattering studies of moderately dense gases. II. Nonhydrodynamic regime *Physical Review A* **25** 481 URL http://doi.org/10.1103/PhysRevA.25.481

[50] Doll U, Burow E, Stockhausen G and Willert C 2016 Methods to improve pressure, temperature, and velocity accuracies of filtered Rayleigh scattering measurements in gaseous flows *Measurement Science and Technology* **27** URL http://doi.org/10.1088/0957-0233/27/12/125204

[51] Pan X, Shneider M N and Miles R B 2002 Coherent Rayleigh-Brillouin scattering *Physical Review Letters* **89**(18) 183001 URL http://doi.org/10.1103/PhysRevLett.89.183001

[52] Zheng Q 2007 Model for polarized and depolarized Rayleigh Brillouin scattering spectra in molecular gases *Optics Express* 14257–14265 URL http://doi.org/10.1364/OE.15.014257

[53] Witschas B, Gu Z and Ubachs W 2014 Temperature retrieval from Rayleigh-Brillouin scattering profiles measured in air *Optics express* **22** 29655—29667 URL http://doi.org/10.1364/oe.22.029655

[54] Liang K, Xu J, Zhang P, Wang Y, Niu Q, Peng L and Zhou B 2017 Temperature dependence of the Rayleigh Brillouin spectrum linewidth in air and nitrogen *Sensors* **17** URL http://doi.org/10.3390/s17071503

[55] Ma Y, Li H, Gu Z, Ubachs W, Yu Y, Huang J, Zhou B, Wang Y and Liang K 2014 Analysis of Rayleigh-Brillouin spectral profiles and Brillouin shifts in nitrogen gas and air *Optics Express* **22** 2092–2104 URL http://doi.org/10.1364/OE.22.002092

[56] Binietoglou I, Giampouras P and Belegante L 2016 Linear approximation of Rayleigh-Brillouin scattering spectra *Applied Optics* **55** 7707–7711 URL http://doi.org/10.1364/AO.55.007707

[57] Witschas B 2011 Analytical model for Rayleigh-Brillouin line shapes in air *Applied Optics* **50** 267–270 URL http://doi.org/10.1364/AO.50.000267

[58] Ma Y, Fan F, Liang K, Li H, Yu Y and Zhou B 2012 An analytical model for Rayleigh-Brillouin scattering spectra in gases *Journal of Optics* **14** 095703 URL http://doi.org/10.1088/2040-8978/14/9/095703

[59] Hunt G J, Ground C R and Hunt R L 2020 Fast approximations of spectral lineshapes to enable optimization of a filtered Rayleigh scattering experiment *Measurement Science and Technology* **31** URL http://doi.org/10.1088/1361-6501/ab8a7e

[60] Miles R B, Forkey J N and Lempert W R 1992 Filtered Rayleigh scattering measurements in supersonic/hypersonic facilities *AIAA 17th Aerospace Ground Testing Conference* URL http://doi.org/10.2514/6.1992-3894

[61] McManus T A and Sutton J A 2019 Quantitative planar temperature imaging in turbulent non-premixed flames using filtered Rayleigh scattering *Applied Optics* **58** URL http://doi.org/10.1364/AO.58.002936

[62] Forkey J N 1996 *Development and Demonstration of Filtered Rayleigh Scattering: a Laser Based Flow Diagnostic for Planar Measurement of Velocity, Temperature and Pressure.* Ph.D. thesis Princeton University

[63] Hoffman D, Münch K U and Leipertz A 1996 Two-dimensional temperature determination in sooting flames by filtered Rayleigh scattering *Optics Letters* **21** URL http://doi.org/10.1364/OL.21.000525

[64] Kearney S P, Schefer R W, Beresh S J and Grasser T W 2005 Temperature imaging in nonpremixed flames by joint filtered Rayleigh and Raman scattering *Applied optics* **44** 1548–1558 URL http://doi.org/10.1364/AO.44.001548

[65] Sutton J A and Patton R A 2014 Improvements in filtered Rayleigh scattering measurements using Fabry-Perot etalons for spectral filtering of pulsed, 532-nm Nd:YAG output *Applied Physics B* **116** 681–698 URL http://doi.org/10.1007/s00340-013-5752-3

[66] Forkey J N, Lempert W R and Miles R B 1997 Corrected and calibrated I_2 absorption model at frequency-doubled Nd:YAG laser wavelengths *Applied Optics* **36** 6729–6738 URL http://doi.org/10.1364/AO.36.006729

[67] Doll U, Stockhausen G and Willert C 2014 Endoscopic filtered Rayleigh scattering for the analysis of ducted gas flows *Experiments in Fluids* **55** URL http://doi.org/10.1007/s00348-014-1690-z

[68] Doll U, Burow E, Beversdorff M, Stockhausen G, Willert C, Morsbach C, Schlüß D and Franke M 2015 The flow field inside a Ranque-Hilsch vortex tube part I: Experimental analysis using planar filtered Rayleigh scattering *9th International Symposium on Turbulence and Shear Flow Phenomena*

[69] Doll U, Stockhausen G and Willert C 2017 Pressure, temperature, and three-component velocity fields by filtered Rayleigh scattering *Optics Letters* **42** URL http://doi.org/10.1364/OL.42.003773

[70] Saltzman A J, Boyda M T, Lowe K T and Ng W F 2019 Filtered Rayleigh scattering for velocity and temperature measurements of a heated supersonic jet with thermal non-uniformity *25th AIAA/CEAS Aeroacoustics Conference* URL http://doi.org/10.2514/6.2019-2677

[71] Doll U, Migliorini M, Baikie J, Zachos P K, Röhle I, Melnikov S, Steinbock J, Dues M, Kapulla R, MacManus D G and Lawson N J 2022 Non-intrusive flow diagnostics for unsteady inlet flow distortion measurements in novel aircraft architectures *Progress in Aerospace Sciences* **130** URL http://doi.org/10.1016/j.paerosci.2022.100810

[72] Komine H, Brosnan S J, Litton A B and Stappaerts E A 1991 Real-time Doppler global velocimetry *29th AIAA Aerospace Sciences Meeting and Exhibit* URL http://doi.org/10.2514/6.1991-337

[73] McGaha C and Reeder M F 2007 Filtered Rayleigh scattering-based concentration measurements for a horizontal buoyant jet *22nd International Congress on Instrumentation in Aerospace Simulation Facilities* URL http://doi.org/10.1109/ICIASF.2007.4380890

[74] Reeder M F, Huffman R E, Branam R D, Lebay K D and Meents S M 2011 Near-field development of gas-phase horizontal laminar jets with positive and negative buoyancy measured with filtered Rayleigh scattering *Experiments in Fluids* **50** 1455–1472 URL http://doi.org/10.1007/s00348-010-0999-5

[75] Yalin A P and Miles R B 2000 Temperature measurements by ultraviolet filtered Rayleigh scattering using a mercury filter *Journal of Thermophysics and Heat Transfer* **14** 210–215 URL http://doi.org/10.2514/2.6510

[76] Zetterberg J, Li Z, Afzelius M and Aldén M 2008 Two-dimensional temperature measurements in flames using filtered Rayleigh scattering at 254 nm *Applied Spectroscopy* **62** URL http://doi.org/10.1366/000370208784909526

[77] Gölz P and Andresen P 1996 Atomic vapor filter for two-dimensional Rayleigh imaging experiments with a narrow-band KrF excimer laser *Applied Optics* **35** 6054–6061 URL http://doi.org/10.1364/AO.35.006054

[78] Mach J and Varghese P L 1999 Velocity measurements by modulated filtered Rayleigh scattering using diode lasers *AIAA Journal* **37** 695–699 URL http://doi.org/10.2514/2.797

[79] Shimizu H, Noguchi K and She C Y 1986 Atmospheric temperature measurement by a high spectral resolution lidar *Applied Optics* **25** 1460–1466 URL http://doi.org/10.1364/AO.25.001460

[80] Gelbwachs J A 1990 422.7-nm atomic filter with superior solar background *Optics Letters* **15** 236–238 URL http://doi.org/10.1364/OL.15.000236

[81] Chan Y C, Tabat M D and Gelbwachs J A 1989 Experimental demonstration of internal wavelength conversion in the magnesium atomic filter *Optics Letters* **14** 722–724 URL http://doi.org/10.1364/OL.14.000722

[82] Miles R B, Yalin A P, Tang Z, Zaidi S H and Forkey J N 2001 Flow field imaging through sharp-edged atomic and molecular 'notch' filters *Measurement Science and Technology* **12** 442–451 URL http://doi.org/10.1088/0957-0233/12/4/308

[83] Forkey J N, Lempert W R and Miles R B 1997 Corrected and calibrated I_2 absorption model at frequency-doubled Nd:YAG laser wavelengths *Applied Optics* **36** 6729–6738 URL

http://doi.org/10.1364/AO.36.006729

[84] Elliot G S, Glumac N and Carter C D 2001 Molecular filtered Rayleigh scattering applied to combustion *Measurement Science and Technology* **12** URL http://doi.org/10.1088/0957-0233/12/4/309

[85] Gustavsson J P R and Segal C 2005 Filtered Rayleigh scattering velocimetry—accuracy investigation in a M=2.2 axisymmetric jet *Experiments in Fluids* **38** 11–20 URL http://doi.org/10.1007/s00348-004-0867-2

[86] Yan B, Chen L, Li M, Chen S, Gong C, Yang F, Wu Y, Zhou J and Mu J 2020 Quantitative temperature imaging at elevated pressures and in a confined space with ch_4/air laminar flames by filtered Rayleigh scattering *Chinese Physics B* **29** URL http://doi.org/10.1088/1674-1056/ab5f00

[87] Forkey J N, Finkelstein N D, Lempert W R and Miles R B 1996 Demonstration and characterization of filtered Rayleigh scattering for planar velocity measurements *AIAA Journal* **34** 442–448 URL http://doi.org/10.2514/3.13087

[88] Finkelstein N D M 1998 *An Ultraviolet laser source and spectral imaging filters for non-intrusive laser-based diagnostics* Ph.D. thesis Princeton University Princeton, NJ

[89] Hain R, Kähler C J and Tropea C 2007 Comparison of ccd, cmos and intensified cameras *Experiments in Fluids* **42** 403–411 URL http://doi.org/10.1007/s00348-006-0247-1

[90] Manin J, Skeen S A and Pickett L M 2018 Performance comparison of state-of-the-art high-speed video cameras for scientific applications *Optical Engineering* **57** URL http://doi.org/10.1117/1.OE.57.12.124105

[91] Elliot G S and Samimy M 1996 Rayleigh scattering technique for simultaneous measurements of velocity and thermodynamic properties *AIAA Journal* **34** URL http://doi.org/10.2514/3.13400

[92] Müller D, Pagel R, Burkert A, Wagner V and Paa W 2014 Two-dimensional temperature measurements in particle loaded technical flames by filtered Rayleigh scattering *Applied Optics* **53** URL http://doi.org/10.1364/AO.53.001750

[93] Allison P M, McManus T A and Sutton J A 2016 Quantitative fuel vapor/air mixing imaging in droplet/gas regions of an evaporating spray flow using filtered Rayleigh scattering *Optics Letters* **41** URL http://doi.org/10.1364/OL.41.001074

[94] Ground C R, Gopal V and Maddalena L 2018 Filtered Rayleigh scattering mixing measurements of merging and non-merging streamwise vortex interactions in supersonic flow *Experiments in Fluids* **59** URL http://doi.org/10.1007/s00348-018-2521-4

[95] Doll U, Dues M, Bacci T, Stockhausen G and Willert C 2018 Aero-thermal flow characterization downstream of an NGV cascade by five-hole probe and filtered Rayleigh scattering measurements *Experiments in Fluids* **59** URL http://doi.org/10.1007/s00348-018-2607-z

[96] Krishna Y, Elbaz A M, Yue Y and Magnotti G 2019 Mole fraction measurement through a transparent quarl burner using filtered Rayleigh scattering *Applied Optics* **58** URL http://doi.org/10.1364/AO.58.005575

[97] Weber V, Brübach J, Gordon R L and Dreizler A 2011 Pixel-based characterization of CMOS high-speed camera systems *Applied Physics B* **103** URL http://doi.org/10.1007/s00340-011-4443-1

[98] Papageorge M J, McManus T A, Fuest F and Sutton J A 2014 Recent advances in high-speed planar Rayleigh scattering in turbulent jets and flames: increased record lengths, acquisition rates, and image quality *Applied Physics B* **115** 197–213 URL http://doi.org/10.1007/s00340-013-5591-2

[99] Beresh S J 2021 Time-resolved particle image velocimetry *Measurement Science and Technology* **32** URL http://doi.org/10.1088/1361-6501/ac08c5

[100] Elliot G S, Glumac N, Carter C D and Nejad A S 1997 Two-dimensional temperature field measurements using a molecular filter based technique *Combustion Science and Technology* **125** URL http://doi.org/10.1080/00102209708935663

[101] McManus T A and Sutton J A 2020 Simultaneous 2d filtered Rayleigh scattering thermometry and stereoscopic particle image velocimetry measurements in turbulent non-premixed flames *Experiments in Fluids* **61** URL http://doi.org/10.1007/s00348-020-02973-z

[102] Most D and Leipertz A 2001 Simultaneous two-dimensional flow velocity and gas temperature measurements by use of a combined particle image velocimetry and filtered Rayleigh scattering technique *Applied Optics* **40** URL http://doi.org/10.1364/AO.40.005379

[103] Dibble R and Hollenbach R 1981 Laser Rayleigh thermometry in turbulent flames *18th Symposium (International) on Combustion* **18** 1489–1499 URL http://doi.org/10.1016/S0082-0784(81)80151-8

[104] Namer I and Scehefer R W 1985 Error estimates for Rayleigh scattering density and temperature measurements in premixed flames *Experiments in Fluids* **3** 1–9 URL http://doi.org/10.1007/BF00285264

[105] Li M, Yan B, Chen L and Chen S 2021 Two-dimensional thermometry measurements in confined swirl flames using filtered Rayleigh scattering *Applied Physics B* **127** URL http://doi.org/10.1007/s00340-021-07615-8

[106] Kearney S P, Beresh S J, Grasser T W, Schefer R W, Schrader P E and Farrow R L 2003 A filtered Rayleigh scattering apparatus for gas-phase and combustion temperature imaging *41st AIAA Aerospace Sciences Meeting and Exhibit* URL https://doi.org/10.2514/6.2003-584

[107] Kearney S P, Beresh S J, Grasser T W, Schefer R W, Schrader P E and Farrow R L 2004 Filtered Rayleigh scattering thermometry in vortex-strained and sooting flames *42nd AIAA Aerospace Sciences Meeting and Exhibit* URL https://doi.org/10.2514/6.2004-1358

[108] Krishna Y, Mahuthannan A M, Luo X, Lacoste D A and Magnotti G 2021 High-speed filtered Rayleigh scattering thermometry in premixed flames through narrow channels *Combustion and Flame* **225** URL http://doi.org/10.1016/j.combustflame.2020.10.053

[109] McManus T A and Sutton J A 2017 Quantitative 2D temperature imaging in turbulent nonpremixed jet flames using filtered Rayleigh scattering *55th AIAA Aerospace Sciences Meeting* URL http://doi.org/10.2514/6.2017-1408

[110] Bergmann V, Meier W, Wolff D and Stricker W 1998 Application of spontaneous Raman and Rayleigh scattering and 2D LIF for the characterization of a turbulent $CH_4/H_2/N_2$ jet diffusion flame *Applied Physics B* **66** URL http://doi.org/10.1007/s003400050424

[111] Witschas B, Vieitez M O, van Duijn E J, Reitebuch O, van de Water W and Ubachs W 2010 Spontaneous Rayleigh-Brillouin scattering of ultraviolet light in nitrogen, dry air, and mosit air *Applied Optics* **49** URL http://doi.org/10.1364/AO.49.004217

[112] Pitts W M and Kashiwagi T 1984 The application of laser-induced Rayleigh light scattering to the study of turbulent mixing *Journal of Fluid Mechanics* **141** 391–429 URL http://doi.org/10.1017/S0022112084000902

[113] Hartfield R J, Abbit J D and McDaniel J C 1989 Injectant mole-fraction imaging in compressible mixing flows using planar laser-induced iodine fluorescence *Optics Letters* **14**(6) 850–852 URL http://doi.org/10.1364/OL.14.000850

[114] Takahashi H, Ikegami S, Oso H, Masuya G and Hirota M 2008 Quantitative imaging of injectant mole fraction and density in supersonic mixing *AIAA Journal* **46** URL http://doi.org/10.2514/1.37783

[115] Gopal V and Maddalena L 2020 Systematic errors in mixing measurements using filtered Rayleigh scattering in supersonic flows *Experiments in Fluids* **61** URL http://doi.org/10.1007/s00348-020-02956-0

[116] Crisanti M, Vergine F and Maddalena L 2014 Filtered Rayleigh scattering measurements in helium-air mixing experiments of selected streamwise vortex interactions in a Mach 2.5 flow *52nd AIAA Aerospace Sciences Meeting* URL http://doi.org/10.2514/6.2014-0984

[117] Ground C, Thumiah D and Maddalena L 2015 Design and application of filtered Rayleigh scattering experiments for mixing studies of new strut injectors for scramjets *31st AIAA Aerodynamic Measurement Technology and Ground Testing Conference* URL

http://doi.org/10.2514/6.2015-2567

[118] Ground C, Viganó D and Maddalena L 2017 Intrusive and non-intrusive quantification of binary mixture composition from strut injectors in supersonic flow *21st AIAA International Space Planes and Hypersonics Technologies Conference* URL http://doi.org/10.2514/6.2017-2167

[119] Ground C, Viganó D and Maddalena L 2018 Comparison of intrusive and non-intrusive mixture composition measurements in supersonic flow *Journal of Propulsion and Power* **34** URL http://doi.org/10.2514/1.B36836

[120] Benhassen F, Polanka M D and Reeder M F 2011 Time resolved filtered Rayleigh scattering measurement of a buoyant jet in a co-flow *49th AIAA Aerospace Sciences Meeting* URL http://doi.org/10.2514/6.2011-1292

[121] Benhassen F, Polanka M D and Reeder M F 2016 Trajectory measurements of a horizontally oriented buoyant jet in a coflow using filtered Rayleigh scattering *Journal of Aerospace Engineering* **30** URL http://doi.org/10.1061/(ASCE)AS.1943-5525.0000655

[122] George J, Jenkins T and Miles R 2014 Diagnosis of high speed flows using filtered Rayleigh scattering *30th AIAA Aerodynamic Measurement Technology and Ground Testing Conference* URL https://doi.org/10.2514/6.2014-2231

[123] Hunt R L, Ground C R, Baurle R A and Danehy P M 2019 Using computational flow imaging to optimize filtered Rayleigh scattering measurements of an isolator shock train *AIAA Propulsion and Energy 2019 Forum* URL https://doi.org/10.2514/6.2019-4016

[124] Feng D, Goldberg B M, Shneider M N and Miles R B 2019 Filtered Rayleigh scattering for pressure measurement applications *AIAA Journal* URL https://doi.org/10.2514/1.J058545

[125] Feng D, Goldberg B M, Shneider M N and Miles R B 2020 Optimization of filtered Rayleigh scattering for the measurement of pressure and temperature *Combustion Science and Technology* URL http://doi.org/10.1080/00102202.2020.1822345

[126] Samimy M and Wernet M P 2000 Review of planar multiple-component velocimetry in high-speed flows *AIAA Journal* **38** URL http://doi.org/10.2514/2.1004

[127] Elliot G S and Beutner T J 1999 Molecular filter based planar Doppler velocimetry *Progress in Aerospace Sciences* **35** URL http://doi.org/10.1016/S0376-0421(99)00008-1

[128] Fischer A 2014 Model-based review of Doppler global velocimetry techniques with laser frequency modulation *Optics and Lasers in Engineering* **93** URL http://doi.org/10.1016/j.optlaseng.2017.01.004

[129] Cadel D R and Lowe K T 2015 Cross-correlation Doppler global velocimetry (CC-DGV) *Optics and Lasers in Engineering* **71** 51–61 URL http://doi.org/10.1016/j.optlaseng.2015.03.012

[130] Forkey J N, Finkelstein N D, Lempert W R and Miles R B 1996 Demonstration and characterization of filtered Rayleigh scattering for planar velocity measurements *33rd AIAA Aerospace Sciences Meeting and Exhibit* URL http://doi.org/10.2514/6.1995-298

[131] Boguszko M and Elliot G 2002 Filtered Rayleigh scattering for fluid/thermal systems *22nd AIAA Aerodynamic Measurement Technology and Ground Testing Conference* URL http://doi.org/10.2514/6.2002-3233

[132] Boguszko M and Elliot G S 2004 Measurements in fluid flows using molecular filter-based techniques *42nd AIAA Aerospace Sciences Meeting and Exhibit* URL http://doi.org/10.2514/6.2004-18

[133] Boguszko M and Elliott G S 2005 On the use of filtered Rayleigh scattering for measurements in compressible flows and thermal fields *Experiments in Fluids* **38** 33–49 URL http://doi.org/10.1007/s00348-004-0881-4

[134] Schroll M, Doll U, Stockhausen G, Meier U, Hassa C W C and Bagchi I 2017 Flow field characterization at the outlet of a lean burn single-sector combustor by laser-optical methods *Journal of Engineering for Gas Turbines and Power* **139** URL http://doi.org/10.1115/1.4034040

[135] Doll U, Stockhausen G, Heinze J, Meier U, Hassa C and Bagchi I 2017 Temperature measurements at the outlet of a lean burn single-sector combustor by laser optical methods *J. Eng. Gas Turbines Power* **139** URL https://doi.org/10.1115/1.4034355

[136] George J, Jenkins T, Grady N, Sutton J and Rice B 2016 Simultaneous multi-property laser diagnostic for high speed flows using filtered Rayleigh scattering *32nd AIAA Aerodynamic Measurement Technology and Ground Testing Conference* URL ttps://doi.org/10.2514/6.2016-3110

[137] Jenkins T P, George J, Feng D and Miles R B 2019 Filtered Rayleigh scattering for instantaneous measurements of pressure and temperature in gaseous flows *AIAA Scitech 2019 Forum* URL https://doi.org/10.2514/6.2019-1324

[138] Feng D, Goldberg B M, Naphade M, Shneider M N and Miles R B 2018 A model study of filtered Rayleigh scattering sensitivity to pressure and temperature *2018 AIAA Aerospace Sciences Meeting* URL https://doi.org/10.2514/6.2018-2042

[139] Feng D, Jenkins T P, Wu Y and George J 2022 Towards simultaneous density and velocity measurements of high-speed flows using filtered Rayleigh scattering *2022 AIAA SciTech Forum* URL https://doi.org/10.2514/6.2022-1314

[140] Boguszko M G 2003 *Measurements in fluid flows using filtered Rayleigh scattering* Ph.D. thesis Rutgers, The State University of New Jersey

[141] Yeaton I J, Maisto P and Lowe K T 2012 Time resolved filtered Rayleigh scattering for temperature and density measurements *28th Aerodynamic Measurement Technology, Ground Testing, and Flight Testing Conference* URL http://doi.org/10.2514/6.2012-3200

[142] Doll U, Röhle I, Dues M and Kapulla R 2022 Time-resolved multi-parameter flow diagnostics by filtered Rayleigh scattering: system design through multi-objective optimisation *Measurement Science and Technology* **33** URL http://doi.org/10.1088/1361-6501/ac7cca

[143] Doll U, Kapulla R, Steinbock J J, Dues M, Migliorini M and Zachos P K 2023 Seeding-free inlet distortion measurement by filtered Rayleigh scattering: diagnostic approach and verification *AIAA SciTech 2023 Forum* URL https://doi.org/10.2514/6.2023-1372

[144] Bevington P R and Robinson D K 2002 *Data reduction and error analysis for the physical sciences* 3rd ed (New York, NY: McGraw-Hill Professional)

[145] Forkey J N, Finkelstein N D, Lempert W R and Miles R B 1995 Control of experimental uncertainties in filtered Rayleigh scattering measurements *33rd AIAA Aerospace Sciences Meeting and Exhibit* URL http://doi.org/10.2514/6.1995-298

[146] Ku H 1966 Notes on the use of propagation of error formulas *Journal of Research of the National Bureau of Standards, Section C: Engineering and Instrumentation* **70C** 263 URL http://doi.org/10.6028/JRES.070C.025

[147] Fahringer T W J, Burns R A, Danehy P M, Bardet P M and Felver J 2020 Pulse-burst cross-correlation doppler global velocimetry *AIAA Journal* **58** 2364–2369 URL https://doi.org/10.2514/1.J059172

[148] Bork B, Böhm B, Heeger C, Chakravarthy S R and Dreizler A 2010 1D high-speed Rayleigh measurements in turbulent flames *Applied Physics B* **101** 487–491 URL http://doi.org/10.1007/s00340-010-4262-9

[149] Patton R A, Gabet K N, Jiang N, Lempert W R and Sutton J A 2012 Multi-kHz temperature imaging in turbulent non-premixed flames using planar Rayleigh scattering *Applied Physics B* **108** 377–392 URL http://doi.org/10.1007/s00340-012-4880-5

[150] Thurow B S, Jiang N, Lempert W R and Samimy M 2005 Development of megahertz-rate planar Doppler velocimetry for high-speed flows *AIAA Journal* **43** 500–511 URL https://doi.org/10.2514/1.7749

[151] Lempert W R, Wu P F and Miles R B 1997 Filtered Rayleigh scattering measurements using a mhz rate pulse-burst laser system *35th AIAA Aerospace Sciences Meeting & Exhibit* URL http://doi.org/10.2514/6.1997-500